


Dissertations and Theses

12-2019

Aerodynamics of the Next Generation Space Weather Prediction Mission

Mark Herring

Follow this and additional works at: <https://commons.erau.edu/edt>

 Part of the [The Sun and the Solar System Commons](#)

This Thesis - Open Access is brought to you for free and open access by Scholarly Commons. It has been accepted for inclusion in Dissertations and Theses by an authorized administrator of Scholarly Commons. For more information, please contact commons@erau.edu.

ASTRODYNAMICS OF THE NEXT GENERATION SPACE
WEATHER PREDICTION MISSION

BY
MARK HERRING

A Thesis

Submitted to the Department of Physical Sciences
and the Committee on Graduate Studies
In partial fulfillment of the requirements
for the degree of
Master in Science in Engineering Physics

12/2019

Embry-Riddle Aeronautical University
Daytona Beach, Florida

© Copyright by Mark Herring 2019
All Rights Reserved

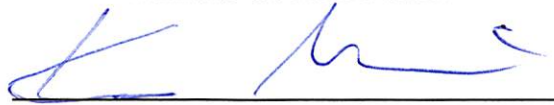
ASTRODYNAMICS OF THE NEXT GENERATION SPACE
WEATHER PREDICTION MISSION

by

Mark Herring

This thesis was prepared under the direction of the candidate's Thesis Committee Chair, Dr. Katariina Nykyri, Professor, Daytona Beach Campus, and Thesis Committee Members Dr. Sergey Drakunov, Professor, Daytona Beach Campus, and Dr. Xuanye Ma, Associate Professor, Daytona Beach Campus, and has been approved by the Thesis Committee. It was submitted to the Department of Physical Sciences in partial fulfillment of the requirements of the degree of Master of Science in Engineering Physics

THESIS COMMITTEE:



Dr. Katariina Nykyri,
Committee Chair



Dr. Sergey Drakunov,
Committee Member



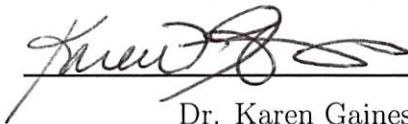
Dr. Xuanye Ma,
Committee Member



Dr. Alan Liu,
Graduate Program Chair,
Engineering Physics



Dr. Terry Oswalt,
Department Chair,
Physical Sciences



Dr. Karen Gaines,
Dean, College of Arts and Sciences



Dr. Christopher Grant,
Associate V.P. for Academics

Abstract

Accurate prediction of the solar wind properties, interplanetary magnetic field direction and various space weather phenomena becomes ever more important as our dependence on Earth orbiting spacecraft increases. Different solar wind drivers can lead both to enhancements and losses of relativistic electrons in the outer radiation belts, thus posing a major risk to satellites. To further our understanding of the Sun's impact on the near Earth space environment, as well as to provide predictive capabilities, a mission placing monitoring satellites in key orbits in the inner Solar System is being proposed. As part of that effort, the possibility of using Libration point orbits for these monitoring satellites is investigated. Using the Circular Restricted Three Body Problem (CRTBP) as an early assessment of transfer trajectories to Libration point orbits around Earth and the other inner planets. Single and multiple shooting methods are implemented and used to find solutions to the equations of motion of the CRTBP targeting periodic orbits and transfer trajectories. Various transfer methods are discussed and Low Energy transfers using invariant manifolds are evaluated. Transfers from Earth to Sun-Earth L1 as well as Sun-Venus, and Sun-Mercury L1 are computed.

Acknowledgments

I would like to thank Dr. Nykyri for her unending patience and support as I worked to develop a working understanding of the dynamics concepts herein. Dr. Xuanye Ma and Dr. Nykyri were both crucial in aiding my understanding of the underlying Space Physics concepts driving this mission. I would also like to thank Dr. Drakunov for kindling my interest in controls and dynamics, and Dr. Udrea for his unwavering support and help with understanding dynamics and astrodynamics concepts required for this research to occur. Without their support and help, I would not have been able to complete this thesis. Finally, I'd like to thank AJ McGahran whose invaluable friendship helped ease the burdens of my final year at Embry-Riddle.

Contents

Abstract	iv
Acknowledgments	v
1 Mission Background and Introduction	1
1.1 Introduction	1
1.2 Effect of Solar Wind on the Near Earth Space Environment	1
1.3 Effect of Solar Wind on Equipment	3
1.3.1 Mission Overview	4
1.4 Lagrange Points History and Missions	5
2 Dynamical Model	11
2.1 Circular Restricted Three Body Problem	11
2.1.1 Equations of Motion	13
2.1.2 Equilibrium Solutions to the CR3BP	18
2.1.3 Stability of libration Points	19
2.2 Invariant Manifolds in the Circular Restricted Three Body Problem	22
3 Computation of Orbits and Transfers	26
3.1 Differential Correction	26
3.2 Single Shooting	28
3.2.1 Constant Time	29
3.2.2 Variable Time	30
3.3 Multiple Shooting	31

3.4	Targeting Halo Orbits	34
3.4.1	Lyapunov	34
3.4.2	Halo Orbits	38
3.4.3	Transfers to Libration Point Orbits	39
4	Conclusion	53
4.1	Implementation	53
4.2	Results and Discussion	53

List of Tables

1.1	Potential locations for satellite deployment in Next Generation Space Weather Prediction mission.	5
1.2	SOHO Halo orbit dimensions [1]	7
1.3	Typical temperature ranges for select spacecraft equipment[2]	9
3.1	Spheres of Influence for select planets.	50
3.2	Velocities for Hohmann Transfers.	52
4.1	Sample of transfers to varying size Halo orbits at Sun-Earth L1	54
4.2	Sample of transfers to varying size Halo orbits at Sun-Venus L1	56
4.3	Sample of transfers to varying size Halo orbits at Sun-Mercury L1	58
4.4	Transfer time and ΔV for Venus and Mercury Halo orbits $A_z = 1000$	58
4.5	Transfer time and ΔV for Venus and Mercury Halo orbits $A_z = 150000$	59

List of Figures

1.1	Libration point locations for a CRTBP	6
1.2	Recreation of SOHO orbit in the CRTBP using differential Correction with the values from Table 1.2 as initial conditions.	7
2.1	Diagram of the non-dimensionalized CRTBP	12
2.2	Top down view of the ecliptic plane. The co-rotating reference frame is in red.	12
2.3	Zero velocity curves in the CRTBP for a Jacobi constant $C =$, the Jacobi constant of L1	17
2.4	Surface plot of the effective potential ($\mu = 0.2$) with libration points shown.	19
2.5	Parametization of a Halo orbit for invariant manifold calculations, $n = 40$	24
2.6	Invariant manifolds of the SOHO L1 Halo orbit	25
3.1	Diagram of idea behind the multiple shooting method.	31
3.2	Lyapunov Orbit calculated using differential correction.	38
3.3	Earth L1 Halo Orbit calculated using differential correction method. .	39
3.4	Jacobi Constant variations during numerical integration with 10^{th} order Runge-Kutta method	41
3.5	Stable manifold of an L2 Halo orbit in the Sun-Earth system	42
3.6	Layout of the weak stability transfer problem.	42
3.7	Close up view of the Earth and the L1 stable manifold.	43
3.8	Stable manifold propagated back to the Poincare section at $y = 0$. .	44

3.9	Poincare map of the stable manifold at $y = 0$. The blue circle is Earth, orange dots are trajectory intersections with the Poincare section . . .	45
3.10	Transfer orbit from Earth parking orbit to Halo at Sun-Earth L1. . .	48
3.11	Transfer orbit from Venus parking orbit to Halo at Sun-Venus L1. . .	48
3.12	Transfer from Earth L1 to Venus L2	49
3.13	Hohmann Transfer	51
4.1	Transfer from Earth parking orbit to L1 Halo, with $A_z = 1,000\text{km}$. .	54
4.2	Transfer from Earth parking orbit to L1 Halo, with $A_z = 50,000\text{km}$.	55
4.3	Transfer from Earth parking orbit to L1 Halo, with $A_z = 150,000\text{km}$	55
4.4	Transfer from Earth parking orbit to L1 Halo, with $A_z = 200,000\text{km}$	56
4.5	Transfer from Venus parking orbit to L1 Halo, with $A_z = 1,000\text{km}$. .	56
4.6	Transfer from Venus parking orbit to L1 Halo, with $A_z = 50,000\text{km}$.	57
4.7	Transfer from Venus parking orbit to L1 Halo, with $A_z = 150,000\text{km}$	57
4.8	Transfer from Venus parking orbit to L1 Halo, with $A_z = 200,000\text{km}$	58
4.9	Transfer from Mercury parking orbit to L1 Halo, with $A_z = 1,000\text{km}$	58
4.10	Transfer from Mercury parking orbit to L1 Halo, with $A_z = 150,000\text{km}$	59

Chapter 1

Mission Background and Introduction

1.1 Introduction

As part of The Next Generation Space Weather Prediction mission, a number of satellites are planned to be deployed to the inner Solar System. These satellites will monitor the Solar Wind in situ, and relay data back to Earth for analysis. The data will be used in an effort to forecast space weather in the Near Earth Space Environment, so as to provide early warning to satellite operators in the hopes of preventing loss or damage of equipment. Satellite locations at various Lagrange/Libration points for Earth, Venus, and Mercury are under consideration. Due to mission time constraints, this thesis will investigate the feasibility of placing satellites in their respective orbits within the required time frame.

1.2 Effect of Solar Wind on the Near Earth Space Environment

The solar wind (SW) is expanding solar atmosphere extending far into the inter-stellar medium [3]. The SW travels radially from the surface of the Sun at speeds between of about 300-700 km/s [4, 5]. The solar wind consists primarily of protons, electrons and helium ions, all of which play a role in the interaction between the solar wind

and the Earth's magnetosphere. As the solar wind leaves the Sun it drags magnetic field lines with it due to the frozen-in plasma condition [4?]. These magnetic field lines make up the interplanetary magnetic field (IMF). The IMF is generally very weak at Earth's orbit, being around 1/1000 of the Earth's own magnetic field. The solar wind properties at Earth's orbit are highly variable, depending on solar activity such as solar flares and coronal mass ejections(CME) [5]. Also, the "quiet" solar wind shows variability and can be divided to "slow" and "fast" solar wind. The high speed SW originates from coronal holes, which appear dark when observed in Extreme Ultraviolet (EUV) and X-ray wave lengths, due to lower plasma density than the surrounding regions. During solar minimum most coronal holes exist at north and south heliographic poles, while at other times more transient holes appear at all latitudes [?]. The equatorial coronal holes are the source of fast plasma that can be directed toward the Earth, so they can be effective drivers of geomagnetic storms. When high speed SW overtakes slow speed SW, it creates regions of very high densities and strong magnetic fields, corotating interaction regions (CIRs) [?].

The exact mechanism generating the magnetic field of the Sun is not well understood, but it is well established that the total number of localized regions of strong magnetic fields, called the sunspots, are known to vary with roughly an 11-year period known as the solar cycle. The peak of the solar cycle is known as solar maximum and is associated with higher solar activity, while the trough is known as solar minimum.

The CMEs are violent eruptions that occur in the solar corona. These eruptions often occur in conjunction with solar flares and hurl huge amounts of plasma and magnetic field lines into interplanetary space [4, 6, 7]. The first indication of a coronal mass ejection is typically X-Rays which arrive at Earth around 8 minutes after the event. The plasma ejected from the suns surface can travel at a significant fraction at of the speed of light, and takes around 1 hour to reach the Earth [6].

The Earth's magnetosphere has several current systems that exist primarily due to energetic particles carried by the solar wind. The main current of concern here is the ring current. It is a westward flow of mostly ions that encircles the Earth [4]. Since the ring current is a closed loop of electrical flow, by Amperes law, it also generates a magnetic field. This magnetic field is in opposition to Earth's own, and

causes degradation of the Earth's magnetic field inside the ring. The actual size of the ring current varies, but it typically exist between 3-6 R_E from Earth [4, 5]. Loss mechanisms keep the ring current in a relative equilibrium condition. However, this equilibrium is disrupted during solar events like fast flows or CMEs.

CMEs and solar flares deposit large amounts of energetic particles into the ring current and Van Allen radiation belts. This results in a drastic increase in the current of the ring current its magnetic field. Variations in the magnetic field are measured on the Earth's surface and are called the Disturbance Storm Time (DsT) index. For example, in 2005 on May 13, a CME impacted the Earth and the DsT decreased to -263 nT [6]. During calm periods, the DST will typically be be around 0 nT or just below[8].

1.3 Effect of Solar Wind on Equipment

Satellites will typically suffer damaging effects from three sources [2], listed below.

- Solar Particle Events (SPE)
- Galactic Cosmic Rays (GCR)
- Trapped Particles

Solar particle events are a result of CMEs and solar flares. These particles will typically result in penetration of shielding designed for defense of background level radiation. Particle energies can be between 50-100 MeV/nucleon, which is considered penetrating. Galactic Cosmic Rays are extra-solar in nature and can have energies up to 1×10^{14} MeV [?].

Earth's inner magnetosphere consists of trapped energetic particle populations that perform gyro, bounce and drift motion in the magnetic field forming the ring current and the Van Allen radiation belts. Electrons are present between 1.5 to 3 R_E , and 3 to 10 R_E [2] and have energies typically between 0.1-10 MeV. The outer radiation belt shows a lot of variability and electrons can be lost by various of processes []. Protons are mainly in the inner ring current and in the inner Van Allen belt, between

1.1 to $3 R_E$ [2], are quite stable and have energies between 10-100 MeV [9]. Electrons are typically non penetrating, instead they cause surface charging and solar panel degradation. Protons, depending on energy can penetrate satellites and cause bulk charging in addition to surface charging. Bulk charging is charging of components and structures inside the satellite. Build up of charge can lead to arcing, which damages electrical components. Depending on the severity of the event, they are classified as the following

- Single Event Upset (SEU)
- Single Event Latchup (SEL)
- Single Event Burnout (SEB)

Single event upsets occur when radiation causes temporary or minor damage such as a bit flip. It is fully recoverable and does not impact operation of the satellite past the time of the event. An SEU causes a component or system to hang, and can disrupt operation. Depending on what the component's function is, it may or may not cause damage that affects the operational capability of the satellite. As the name suggest, and SEB causes permanent and irreversible damage to a component and may even result in a loss of the satellite [2].

All space weather is driven by solar activity, which is tracked by counting the number of sun spots on the solar surface. Sun spots appear as dark areas on the sun, and are relatively cool [4]. The National Oceanic and Atmospheric Administration(NOAA) tracks and publishes this data.

In 2013, Lohmeyer and Baker [10] studied the correlation between space weather and GEO communication satellite anomalies. They noted that seventeen out of twenty six anomalies occurred within two weeks of a severe space weather event.

1.3.1 Mission Overview

The Next Generation Space Weather Prediction mission has a tentative time line of 2032-2038. This time period coincides with the predicted [11] rise to solar maximum as

well as solar minimum. The primary goal is to develop understanding of the dynamics in the vicinity of libration point orbits, as well as the methods used to calculate those orbits. Additionally, transfer trajectories from the secondary bodies (Earth, Venus, and Mercury) of the CRTBP to their respective L1 points are developed. Considering the time constraints of the mission, it is of interest to determine whether transfers to these points can be achieved in a reasonable amount of time.

Planet	Libration Points
Earth	L1
Venus	L1,L3,L4,L5
Mercury	L1,L3,L4,L5

Table 1.1: Potential locations for satellite deployment in Next Generation Space Weather Prediction mission.

1.4 Lagrange Points History and Missions

Libration points are equilibrium points in the Circular Restricted Three Body Problem (CRTBP). The CRTBP considers three bodies, two large and one infinitesimally small. Three of the Lagrange points (L1, L2, and L3) are co-linear on a line drawn between the two large bodies, and the remaining two (L4, L5) are located as shown in Figure 1.1. Though named after Lagrange, the co-linear Lagrange points were discovered by Leonhard Euler who published his findings in 1767[12, 13]. The two remaining points, called the triangular libration points were discovered by Lagrange in 1772[12, 14].

There have been a number of missions to libration points, beginning with ISEE-3 (International Sun-Earth Explorer). [15]. The primary goal of the ISEE-3 mission was upstream monitoring of the solar wind. Since the spacecraft was initially stationed at the Sun-Earth L1 point, it was able to provide solar wind data to scientists on Earth one hour before the solar wind impacted the Earth's magnetosphere [15]. ISEE-3 orbited the Sun-Earth L1 in a quasi-periodic orbit with a z amplitude of approximately 120,000 km [15, 16]. The orbit was chosen for primarily for two reasons;

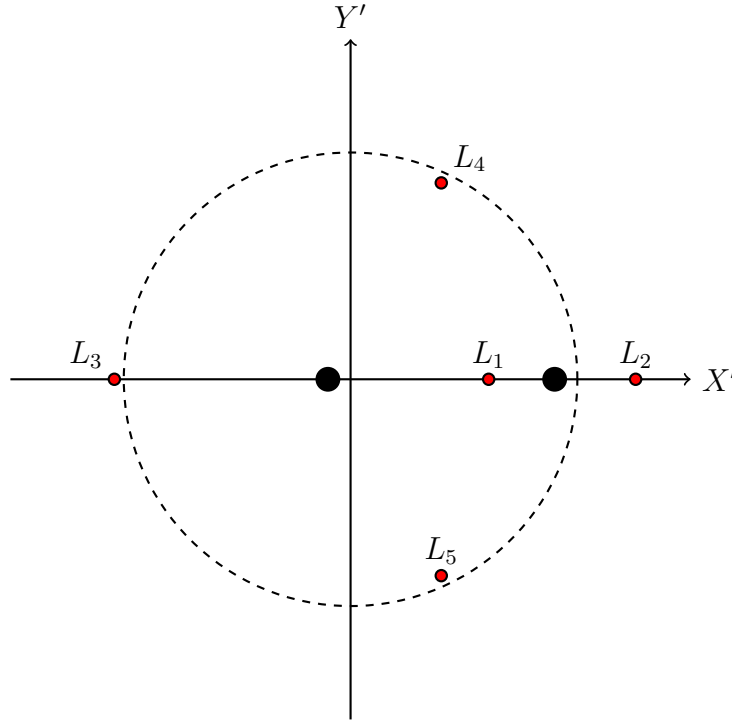


Figure 1.1: Libration point locations for a CRTBP

larger Halo orbits require less ΔV (change in velocity) for orbit insertion, and the size of the orbit prevent the ISEE-3 spacecraft from experiencing down link interference from solar radiation [15, 16]. Design of the orbit requires several steps. First, a third order analytical approximation is used to find approximate initial conditions [16, 17]. The analytical orbit is constructed by setting a desired z amplitude (A_z), the x amplitude follows as a consequence of the dynamics near the libration point. With relatively good initial conditions obtained, a differential correction process is used to numerical correct the analytically obtained initial conditions. The numerically corrected orbit had lower ΔV maintenance requirements and was therefore chosen as the orbit for the actual mission. Richardson [16, 17] reported that the average stationkeeping ΔV was around 10m/s/yr. The third order analytical approximation and numerical differential correction methods are discussed in 3.1.

The next mission to a libration point was 18 years later, in 1995 [15, 18]. The Solar and Heliospheric Observatory(SOHO) was launched in December 1995 and Halo

orbit insertion took place in February 1996. As with the ISEE-3 mission, SOHO had to avoid interference from the Sun in order to communicate with earth; this led to similar orbit to ISEE-3 [1].

A_x (km)	A_y (km)	A_z (km)	T (days)
206,448	666,672	120,100	178

Table 1.2: SOHO Halo orbit dimensions [1]

This particular type of orbit is referred to as Class 2 or southern Halo orbit [1, 17]. Figure 1.2 demonstrates the geometry of this type of orbit. Specifically, the orbit projection in the $X - Z$ plane indicates that the orbit trajectory stays behind (Earth side) and under ($-Z$) the L1 point.

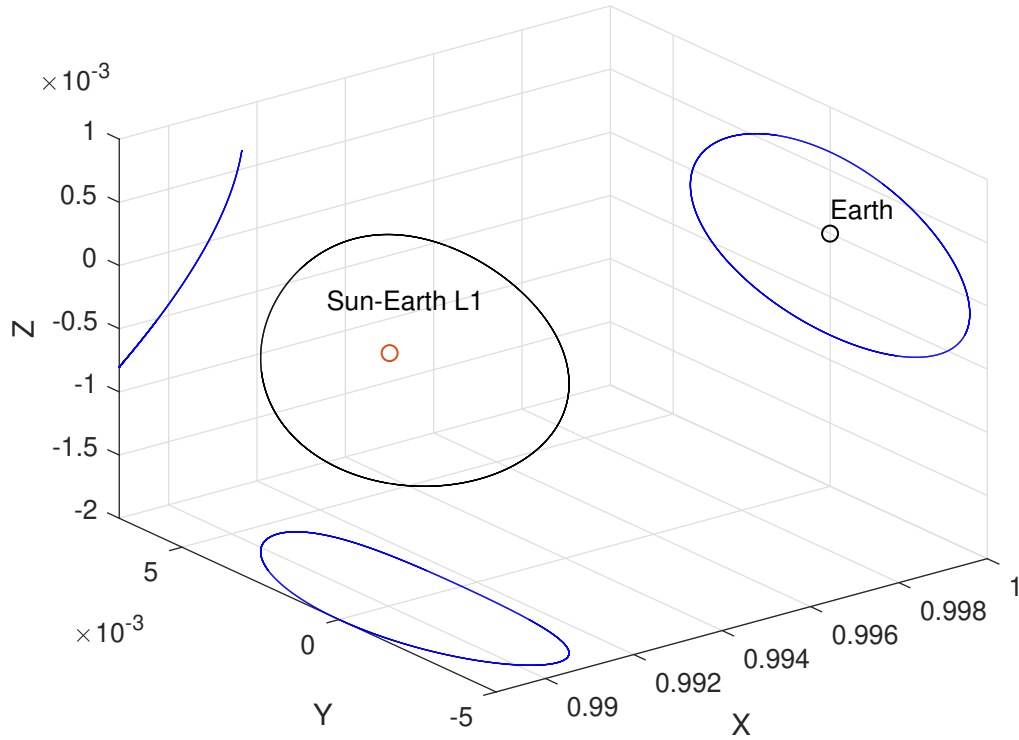


Figure 1.2: Recreation of SOHO orbit in the CRTBP using differential Correction with the values from Table 1.2 as initial conditions.

Between 1996 and 1998, the SOHO spacecraft used an average ΔV of 2.4m/s/yr

[1], a significantly lower value than the average yearly ΔV used by ISEE-3. The inherent risk of using libration point orbits is highlighted by SOHO, which experienced two distinct system failures during its mission [1]. Due to the saddle point nature of the co-linear libration points, small perturbations in the orbit lead to exponential departures (see 2.1.3 and 2.2). Typically these perturbations are accounted for using station keeping maneuvers which impart small but necessary ΔV to the spacecraft. Depending on the direction of the perturbation, the spacecraft can escape towards the sun and enter a heliocentric orbit. Conversely, the spacecraft could escape towards Earth. Therefore it is critical that stationkeeping maneuvers are performed as accurately and precisely as possible.

As mentioned previously, ΔV requirements for Halo orbit increase as the Halo orbit size decreases. For example, the Advance Composition Explorer(ACE) which was launched in 1997, had a much smaller Halo orbit than ISEE-3 and SOHO. Its halo orbit insertion ΔV was therefore much higher; between 140m/s and 200m/s [19]. Both ISEE-3 and SOHO used direct transfers to reach their respective Halo orbits, and while ACE eventually used the same, the possibility of using a Lunar gravity assist was considered. The Lunar gravity assist would have required highly elliptic phasing orbits, and ACE would have passed through the Van-Allen radiation belts several times. In the end, due to those reasons and optimization constraints, a direct transfer was selected [19].

While the previous missions have all worked backwards from orbit design, the HERSCHEL/PLANCK missions designed their L2 Lissajous orbits based on launch vehicle constraints. The two main constraints from the launch vehicle were low perigee altitude, and a line of apsides near the equator; the last due to the launch site being near the equator. Other orbit design constraints included eclipse avoidance and a mission time of 6 years [20]. In order to meet the launch constraints, various Lissajous orbits and their stable manifolds were investigated. As with previous missions, the investigation began with an analytical approximation and followed with a some numerical method. In this case, the numerical method was the bisection root-finding method. This was used to find the intersection at perigee with the Lissajous stable manifolds [20].

Orbits about libration points are chosen for a variety of reasons. However, recurring requirements through all of the missions above are the following.

- Stable thermal environment
- Continuous line of site with science target
- Eclipse avoidance

Equipment on board is designed to operate within specific thermal tolerances. Table 1.3 provides some examples of temperature ranges that spacecraft equipment must stay within.

Component	Temperature Ranges (°C)	
	Operational	Survival
Batteries	0 to 15	-10 to 25
Reaction Wheels	-10 to 40	-20 to 50
Solar Panels	-150 to 110	-200 to 130
Gyros/IMUs	0 to 40	-10 to 50
Star Trackers	0 to 30	-10 to 40
Antennas	-100 to 100	-120 to 130

Table 1.3: Typical temperature ranges for select spacecraft equipment[2]

Spacecraft are equipped with a thermal control subsystem; which is responsible for ensuring that all thermal constraints are met. Two general categories of thermal control exist; active and passive. Passive means are usually preferred, as they rely on natural thermal radiation to remove heat from the spacecraft and therefore require no power [2]. For example, a satellite in zero inclination low Earth orbit(LEO) will spend half its orbit in Earth's shadow. Whatever thermal equilibrium was maintained while in direct sunlight will be upset and the thermal control system will have to add heat to the spacecraft to keep its components within their operating limits. A properly designed libration point orbit avoids this particular problem entirely. At the L1 point the satellite will be exposed to essentially constant thermal radiation from the sun. Although, as is the case with HERSCHEL/PLANCK spacecraft, an L2 orbit can also be thermally stable if it is properly designed to avoid eclipsing. Thermal stability

reduces the load on the spacecrafts thermal control subsystem, as well as minimizes temperature transients.

The other points are very mission specific. For example line of sight with the science target greatly depends on the science that is being performed. In this case, the spacecraft are being placed such that they are able to perform in situ measurements of the solar wind as it flows radially from the Sun.

Chapter 2

Dynamical Model

2.1 Circular Restricted Three Body Problem

The Circular Restricted Three Body Problem (CRTBP) is a specialization of the Three Body Problem (TBP). The TBP considers the motion of three bodies under the influence of each others gravitational forces [21]; with no restrictions or assumptions on orbit shape or the masses of the bodies. The CRTBP restricts the mass of one of the bodies to be so small as to have an inconsequential effect on the remaining two, which orbit their common barycenter in perfect circular orbits. The equations of motion in the Primary-Secondary co-rotating reference frame, $[X', Y', Z']$ are considered. In this frame, the primary and secondary bodies lie on the X' axis. The Y' axis is in the plane of motion and the Z' axis is coincident with the inertial Z as shown in Figure 2.1. The entire frame rotates about Z and Z' with a constant angular velocity equal to the angular velocity of the primary and secondary bodies.

Transformation of the position vector from the rotating reference frame to the inertial reference frame is accomplished using a simple transformation matrix. Since the entire frame rotates about the Z axis, the transformation is accomplished with $\mathbf{r} = \mathbf{R}_z \mathbf{r}'$. Velocity rotation requires the derivative of \mathbf{R}_z , which takes the form shown

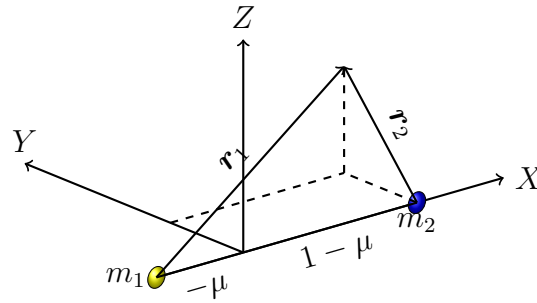


Figure 2.1: Diagram of the non-dimensionalized CRTBP

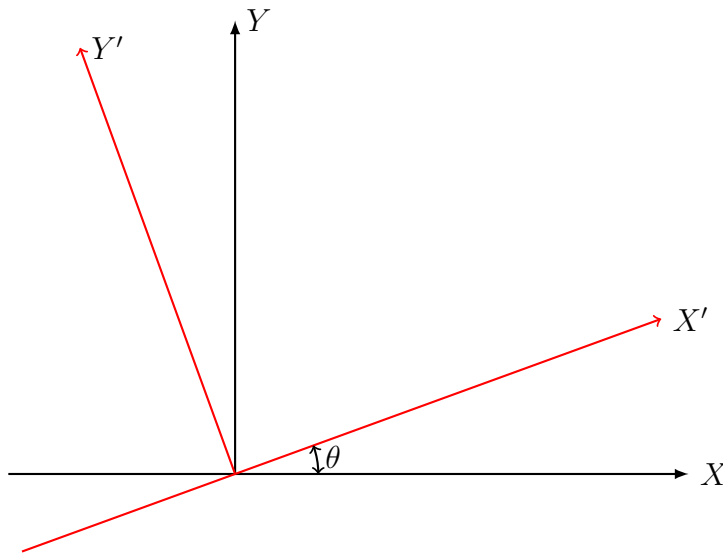


Figure 2.2: Top down view of the ecliptic plane. The co-rotating reference frame is in red.

below.

$$\mathbf{R}_z(\theta) = \begin{bmatrix} \cos \theta & -\sin \theta & 0 \\ \sin \theta & \cos \theta & 0 \\ 0 & 0 & 1 \end{bmatrix}, \quad (2.1)$$

where $\theta = nt^*$ and n is the mean motion and t^* is the non-dimensional time.

$$\left. \frac{d\mathbf{R}'}{dt} \right|_i = \left. \frac{d\mathbf{R}'}{dt} \right|_R + [\omega_\times] \mathbf{R} \quad (2.2)$$

Equation 2.2 is the general form where $[\omega_\times]$ is the skew symmetric matrix shown in Equation 2.3. In the rotating frame, $\left. \frac{d\mathbf{R}'}{dt} \right|_R = 0$, thus the equation reduces to $[\omega_\times] \mathbf{R}$. Since we are concerned only with rotation about the Z axis, $\mathbf{R} = \mathbf{R}_z$ in this case.

$$[\omega_\times] = \begin{bmatrix} 0 & -\omega_z & \omega_y \\ \omega_z & 0 & -\omega_x \\ -\omega_y & \omega_x & 0 \end{bmatrix} \quad (2.3)$$

Therefore, the rotation of the velocity vector from the co-rotating reference frame to the inertial frame is expressed as

$$\mathbf{v} = [\omega_\times] \mathbf{R} \mathbf{v}. \quad (2.4)$$

Because there is no rotation about any axis except for Z , $\omega_x = \omega_y = 0$.

2.1.1 Equations of Motion

The equations of motion for the CRTBP are well known [12, 21]. In both the numerical and analytic cases the problem is non-dimensionalized for ease of analysis. Three quantities require non dimensionalization: position, velocity, and time. The relationships between these quantities and their dimensional counterparts are given below. In this notation, the $*$ term designates quantities with dimensional units.

$$x = \frac{x^*}{a} \quad (2.5)$$

$$\dot{x} = \dot{x}^* \sqrt{\frac{GM_p + GM_s}{a}} \quad (2.6)$$

$$t = t^* \sqrt{\frac{a}{GM_p + GM_s}} \quad (2.7)$$

In the non-dimensional problem, the distance between the two bodies is normalized to unity. As can be seen in Figure 2.1, this results in the primary body being offset from the origin by a quantity $-\mu$. The value of μ is calculated from masses or gravitational parameters of the primary and secondary body.

$$\mu = \frac{m_2}{m_1 + m_2} \quad (2.8)$$

$$\mu = \frac{\mu_2}{\mu_1 + \mu_2} \quad (2.9)$$

Where μ_1 and μ_2 are the Gravitational parameters of the primary and secondary bodies, respectively.

$$r_1 = \sqrt{(x + \mu)^2 + y^2 + z^2} \quad (2.10)$$

$$r_2 = \sqrt{(x - 1 + \mu)^2 + y^2 + z^2} \quad (2.11)$$

$$(2.12)$$

$$\ddot{x} = 2\dot{y} - U_x \quad (2.13)$$

$$\ddot{y} = 2\dot{x} - U_y \quad (2.14)$$

$$\ddot{z} = U_z \quad (2.15)$$

Here, U is the potential function in Equation 2.16, and the subscript represents the partial derivative with respect to that variable.

$$U = \frac{1}{2}[x^2 + y^2 + z^2 + \mu(1 - \mu)] + \frac{1 - \mu}{r_1} + \frac{\mu}{r_2} \quad (2.16)$$

$$\ddot{x} = 2\dot{y} - (1 - \mu)\frac{x + \mu}{r_1^3} - \mu\frac{x + \mu - 1}{r_2^3} \quad (2.17)$$

$$\ddot{y} = 2\dot{x} - (1 - \mu)\frac{y}{r_1^3} - \mu\frac{y}{r_2^3} \quad (2.18)$$

$$\ddot{z} = (1 - \mu)\frac{z}{r_1^3} - \mu\frac{z}{r_2^3} \quad (2.19)$$

$$(2.20)$$

The problem has no closed form solution, but several analytic approximations exist. Most notably, the third order approximation by Richardson [17] shown in Equations 2.21 - 2.23. The $a_{i,j}$, $b_{i,j}$, and $d_{i,j}$ terms are constants computed based on equations given in [17]. A_z , and A_x are the x and z amplitudes of the orbit, and are related by the phase constraint relationship 2.24.

$$x = a_{21}A_x^2 + a_{22} - A_x \cos \tau_1 + (a_{23}A_x^2 - a_{24}A_z^2) \cos 2\tau_1 \quad (2.21)$$

$$y = kA_x \sin \tau_1 + (b_{21}A_x^2 - b_{22}A_z^2) \sin 2\tau_1 \quad (2.22)$$

$$z = \delta_n A_z \cos \tau_1 + \delta_n d_{21} A_x A_z (\cos 2\tau_1 - 3) \quad (2.23)$$

$$+ \delta_n (d_{32} A_z A_x^2 - d_{31} A_z^3) \cos 3\tau_1$$

$$l_1 A_x^2 + l_2 A_z^2 + \Delta = 0 \quad (2.24)$$

The terms l_1 , l_2 , and Δ are constants. See [17] for a full list of constants and their equations. As the CRTBP is a chaotic system, it is imperative that good

approximations are used for the initial conditions of the numerical scheme used to solve them. The Richardson approximation is often used to generate a set of initial conditions, which are then fed into a differential correction scheme to refine.

The equations of motion admit an energy integral, called the Jacobi integral. The Jacobi integral is related to the energy of the system by [12, 22]. Energy of the system bounds the realms of possible motion in the CRTBP, which is given by

$$C = -2E. \quad (2.25)$$

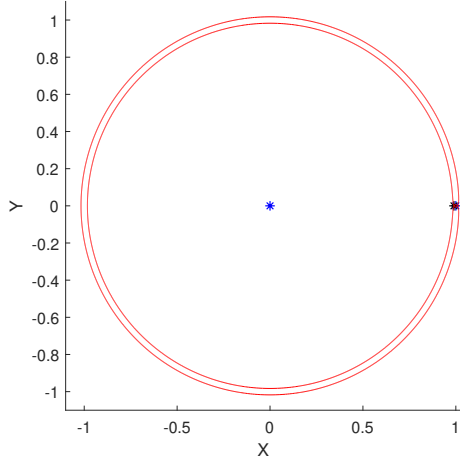
Here, the energy of the system E can be represented as

$$E(x, y, z, \dot{x}, \dot{y}, \dot{z}) = \frac{1}{2}(\dot{x}^2 + \dot{y}^2 + \dot{z}^2) + U(x, y, z), \quad (2.26)$$

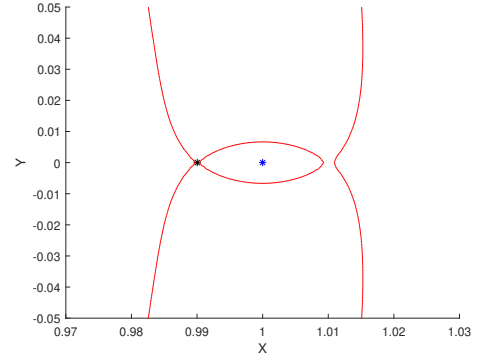
Where U is the effective potential from Equation 2.16. If the phase space of system is \mathbb{R}^n , then the Jacobi constant represents an $n - 1$ energy manifold embedded in that phase space [12, 22]. The manifold, $\mathcal{M}(\mu, E = \{(x, y, z) | E(x, y, z, \dot{x}, \dot{y}, \dot{z})\})$, bounds the realms of possible motion for a given constant μ and E . The realms of possible motion are called Hill's regions, and are typically represented by projecting the $n - 1$ manifold into position space. The boundary's of the energy manifold are called zero velocity curves.

As an object approaches a zero velocity curve its kinetic energy approaches zero and it can never cross. Because of this, inside the region bounded by the zero velocity curves is called the forbidden region [12, 22]. Due to the relationship in Equation 2.25, as the Jacobi energy increases, the energy of the system decreases.

The equations of motion can also be written in Hamiltonian form. The conjugate momenta are written as in Equation 2.30. The Hamiltonian is shown in Equation 2.31



(a) Zero velocity curve, entire CRTBP system with the Primary body at the center.



(b) Zero velocity curve, zoomed in on the secondary body.

Figure 2.3: Zero velocity curves in the CRTBP for a Jacobi constant $C =$, the Jacobi constant of L1

$$p_x = \dot{x} - y \tag{2.27}$$

$$p_y = \dot{y} + x \tag{2.28}$$

$$p_z = \dot{z} \tag{2.29}$$

$$\tag{2.30}$$

$$H(x, y, z, p_x, p_y, p_z) = \frac{1}{2}((p_x + y)^2 + (p_y - x)^2) + p_z^2 \frac{1 - \mu}{r_1} - \frac{\mu}{r_2} \tag{2.31}$$

The Jacobi constant and Hamiltonian are related by

$$C = -2H + \mu(1 - \mu) \tag{2.32}$$

2.1.2 Equilibrium Solutions to the CR3BP

In order to locate the libration points, first assume that they are in the plane of motion shared by the two bodies; i.e., $z = 0$. If the co-linear libration points are of interest, then we can further assume that $y = 0$. Because the libration points are equilibrium points in the CRTBP, their position is constant. From this we can deduce that the velocity and accelerations are all zero. Applying these assumptions to the equations of motion completely eliminates two of the ODEs. From the remaining equation, three separate quintic polynomials can be found; the zeros of which correspond to the co-linear libration points [21].

Locating the triangular libration points, L4 and L5, is a matter of solving the equations of motion with an equilibrium assumption above as well as $z = 0$. This results in the expression below, which can be solved for x and y .

$$0 = - (1 - \mu) \frac{x + \mu}{r_1^3} - \mu \frac{x + \mu - 1}{r_2^3} \quad (2.33)$$

$$0 = - (1 - \mu) \frac{y}{r_1^3} - \mu \frac{y}{r_2^3} \quad (2.34)$$

The triangular libration points are then located at the following x and y coordinates.

$$x = -\mu + \frac{1}{2} \quad (2.35)$$

$$y = \pm \frac{\sqrt{3}}{2} \quad (2.36)$$

The locations of all libration points are illustrated in Figure 1.1. Since periodic orbits about the libration points are of interest, it is necessary to investigate stability of the equilibrium solutions.

$$0 = (1 - \mu) \frac{x + \mu}{(x + \mu)^3} - \mu \frac{x + \mu - 1}{(x + \mu - 1)^3} \quad (2.37)$$

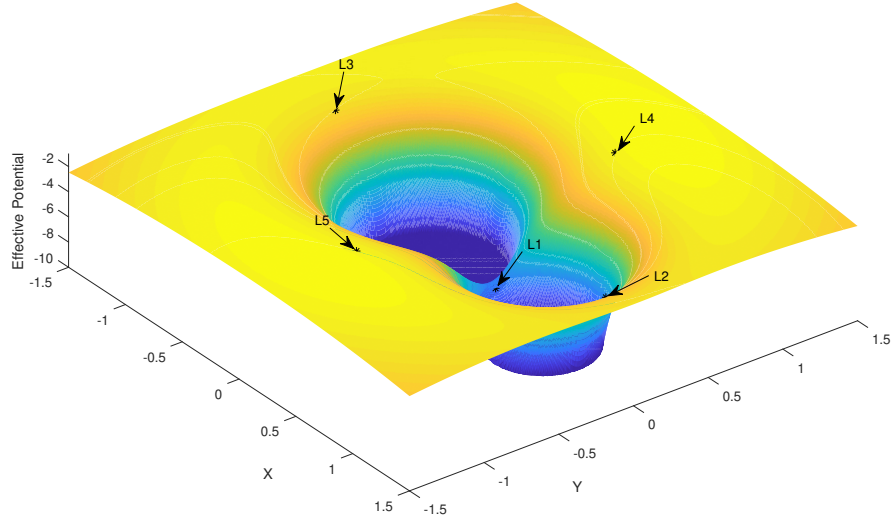


Figure 2.4: Surface plot of the effective potential ($\mu = 0.2$) with libration points shown.

Figure 2.4 illustrates the effective potential in the CRTBP. The two potential wells are from the primary and secondary bodies, with the smallest (in diameter) being the secondary. The saddle point nature of the L1 libration point can be seen from the geometry of the effective potential. L1 is located on the neck between the two bodies.

2.1.3 Stability of libration Points

Stability of is investigated by linearizing Equations 2.20 about the equilibrium points of the system. Consider the dynamical system

$$\frac{dx}{dt} = f(x) \quad (2.38)$$

A Taylor expansion about the equilibrium point x_{eq} , neglecting higher order terms is as follows:

$$\frac{dx}{dt} = f(x) \Big|_{x_{eq}} + \frac{\partial f}{\partial x} \Big|_{x_{eq}} x \quad (2.39)$$

The derivative term $\frac{\partial f}{\partial x}$ is the \mathbf{A} matrix from the linear system.

$$\dot{\mathbf{x}} = \mathbf{A}\mathbf{x} \quad (2.40)$$

The equations of motion for the CRTBP can be expressed in state space form as

$$\begin{bmatrix} \dot{x} \\ \dot{y} \\ \dot{z} \\ \ddot{x} \\ \ddot{y} \\ \ddot{z} \end{bmatrix} = \begin{bmatrix} F_1 \\ F_2 \\ F_3 \\ F_4 \\ F_5 \\ F_6 \end{bmatrix} = \begin{bmatrix} \dot{x} \\ \dot{y} \\ \dot{z} \\ 2\dot{y} + x + \frac{(\mu-1)(\mu+x)}{[(\mu+x)^2+y^2+z^2]^{\frac{3}{2}}} - \frac{\mu(\mu+x-1)}{[(\mu+x-1)^2+y^2+z^2]^{\frac{3}{2}}} \\ -2\dot{x} + y + \frac{(\mu-1)y}{[(\mu+x)^2+y^2+z^2]^{\frac{3}{2}}} - \frac{\mu y}{[(\mu+x-1)^2+y^2+z^2]^{\frac{3}{2}}} \\ \frac{(\mu-1)z}{[(\mu+x)^2+y^2+z^2]^{\frac{3}{2}}} - \frac{\mu z}{[(\mu+x-1)^2+y^2+z^2]^{\frac{3}{2}}} \end{bmatrix} \quad (2.41)$$

Since the \mathbf{A} matrix is the Jacobian of the equations of motion, it has the form

$$\mathbf{A} = \begin{bmatrix} \frac{\partial F_1}{\partial X} & \frac{\partial F_1}{\partial Y} & \frac{\partial F_1}{\partial Z} & \frac{\partial F_1}{\partial \dot{X}} & \frac{\partial F_1}{\partial \dot{Y}} & \frac{\partial F_1}{\partial \dot{Z}} \\ \frac{\partial F_2}{\partial X} & \ddots & & & & \vdots \\ \vdots & & \ddots & & & \vdots \\ \vdots & & & \ddots & & \vdots \\ \vdots & & & & \ddots & \vdots \\ \frac{\partial F_n}{\partial X} & \dots & \dots & \dots & \dots & \frac{\partial F_n}{\partial \dot{Z}} \end{bmatrix} \quad (2.42)$$

The \mathbf{A} matrix can be broken into four sub-matrices.

$$\mathbf{A} = \begin{bmatrix} \mathbf{0} & \mathbf{I} \\ \mathbf{U} & \mathbf{\Omega} \end{bmatrix} \quad (2.43)$$

Here $\mathbf{\Omega}$ has the form shown below, and \mathbf{U} contains partial derivatives of the equations of motion.

$$\mathbf{\Omega} = \begin{bmatrix} 0 & 2 & 0 \\ -2 & 0 & 0 \\ 0 & 0 & 0 \end{bmatrix} \quad (2.44)$$

At this point, to evaluate the stability of the Libration points for a given CRTBP, the positions of the points are inserted and the eigenvalues of the matrix are calculated. For example, let us next consider the L1 point in the Sun-Earth CRTBP. The mass parameter for this system is $\mu = 3.00348727176121 \times 10^{-6}$, and L1 has coordinates of $[0.990026615575206, 0, 0]^T$.

$$\mathbf{U}_{SEL1} = \begin{bmatrix} 9.1216977095219 & 0 & 0 \\ 0 & -3.060848854760950 & 0 \\ 0 & 0 & -4.06084885476095 \end{bmatrix} \quad (2.45)$$

The eigenvalues of the \mathbf{A} matrix are

$$\begin{bmatrix} \lambda_1 \\ \lambda_2 \\ \lambda_3 \\ \lambda_4 \\ \lambda_5 \\ \lambda_6 \end{bmatrix} = \begin{bmatrix} -2.53256975999929 \\ 2.53256975999929 \\ -1.24900009027033 \times 10^{-16} + 2.0869898737081i \\ -1.24900009027033 \times 10^{-16} - 2.0869898737081i \\ 0 + 2.0151547967243i \\ 0 - 2.0151547967243i \end{bmatrix} \quad (2.46)$$

Since λ_1 and λ_2 are real and opposite in sign, we can conclude that L1 is a saddle point. This is true for all the three co-linear libration points.

2.2 Invariant Manifolds in the Circular Restricted Three Body Problem

[23] defines the invariant manifolds of the CRTBP as the set of all the 6-dimensional vectors that converge to a given periodic orbit in forward and backwards time [23]:

$$\mathcal{M}(C_h) = \{(x, y, z, \dot{x}, \dot{y}, \dot{z}) : C(x, y, z, \dot{x}, \dot{y}, \dot{z}) = C_h\} \quad (2.47)$$

Here $\mathcal{M}(C_h)$ is a five dimensional manifold embedded in six dimensional phase space. When projected into three dimensional position space, the manifolds exhibit tube-like structures that extend from periodic solutions to the CRTBP equations of motion. In order to calculate invariant manifolds, the Monodromy matrix is typically used to push a perturbation vector around the periodic solution. Consider again the dynamical system in Equation 3.1. Let T be the period of the periodic solution. If that system has a solution $\mathbf{x}(T)$ that follows from some initial condition $\mathbf{x}(0)$, then the flow map is a solution to that system 3.2. If the initial condition is perturbed by $\delta\mathbf{x}_0$ then the change in the final state $\mathbf{x}(T)$ is

$$\delta\mathbf{x}(T) = \phi(T, \mathbf{x}_0 + \delta\mathbf{x}_0) - \phi(T, \mathbf{x}_0) \quad (2.48)$$

Again, using a Taylor series expansion

$$\delta\mathbf{x}(T) = \Phi(T)\delta\mathbf{x}_0, \quad (2.49)$$

which is typically referred to as the state transition matrix. However, because it now represents the flow mapping to a periodic orbit of period T , it is called the Monodromy matrix[12, 21]. The Monodromy matrix has information about the stability of the orbit.

$$\mathbf{M} = \Phi(T) \quad (2.50)$$

Since the Equation 2.49 is a solution to the variational equations, it is also a solution to the normal dynamical equations:

$$\dot{\mathbf{x}}(t) = \mathbf{Df}(\mathbf{x}(t))\mathbf{x}(t) \quad (2.51)$$

The monodromy matrix has the following eigenvalues:

$$\begin{bmatrix} \lambda_1 \\ \lambda_2 \\ \lambda_3 \\ \lambda_4 \\ \lambda_5 \\ \lambda_6 \end{bmatrix} \quad (2.52)$$

For a periodic solution to the dynamical equations, the monodromy matrix will have two real eigenvalues:

$$\lambda_1 = \frac{1}{\lambda_2} \quad (2.53)$$

$$\lambda_1, \lambda_2 \in \mathbb{R} \quad (2.54)$$

Where λ_1 is the largest eigen value and its inverse is the smallest. The remaining eigenvalues are complex numbers representing the periodic motion of the solution. In the case of a Lyapunov orbit, two of the eigen values take on $\lambda_3 = \lambda_4 = 1$, which follows from the orbit not having any motion in the Z direction.

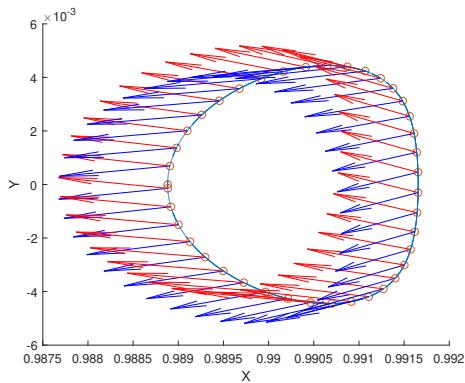
The eigenvalue λ_1 also has the property $|\lambda_1| > 1$ and corresponds to an eigen

vector $\boldsymbol{\lambda}_u$, which represents a tangential perturbation away from the periodic solution. In order to calculate the invariant manifolds of a periodic solution, a perturbation vector is constructed along the direction of the stable and unstable eigenvectors. This perturbation vector v_p must be calculated at each point of interest along the orbit. A set of initial conditions for the invariant orbits is generated using the stable and unstable perturbations[12, 21]

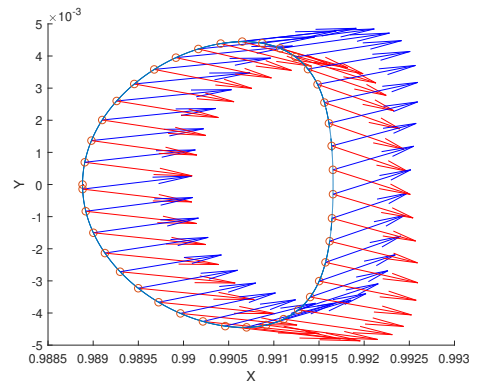
$$\mathbf{x}_{p,s}(n) = \mathbf{x}(n) \pm \epsilon \boldsymbol{\lambda}_s \quad (2.55)$$

$$\mathbf{x}_{p,u}(n) = \mathbf{x}(n) \pm \epsilon \boldsymbol{\lambda}_u, \quad (2.56)$$

where $\mathbf{x}_{p,s}(n)$ is the n th point of parametrization along the orbit. $\boldsymbol{\lambda}_s$ and $\boldsymbol{\lambda}_u$ are the stable and unstable eigenvectors of the Monodromy matrix, respectively. A scaling factor ϵ is used to offset the point from the orbit, the number used is rather arbitrary. Typically recommended numbers are on the order of 10^{-6} , which in the CRTBP corresponds to a distance of around 1000km. The order of ϵ must be small enough that the linear approximation still holds [21, 24]. Figure 2.5 illustrates these perturbations applied to the SOHO L1 Halo orbit. Once the initial conditions are obtained, the stable invariant manifolds can be found by numerically integrating backwards in time. The unstable manifolds are integrated in forward time.



(a) Directions of positive stable(blue) and unstable(red) perturbations along a Halo orbit.



(b) Directions of negative stable(blue) and unstable(red) perturbations along a Halo orbit.

Figure 2.5: Parametization of a Halo orbit for invariant manifold calculations, $n = 40$

Figure 2.6 shows the stable (blue) and unstable (red) invariant manifolds for the SOHO orbit. The perturbed initial conditions are propagated to the Poincare section which is a plane at $y = 0$ to the $+x$ side of the Earth. Any spacecraft placed on the stable manifold will asymptotically converge to the Halo orbit. Conversely, any spacecraft placed on the unstable manifold will asymptotically diverge from the orbit.

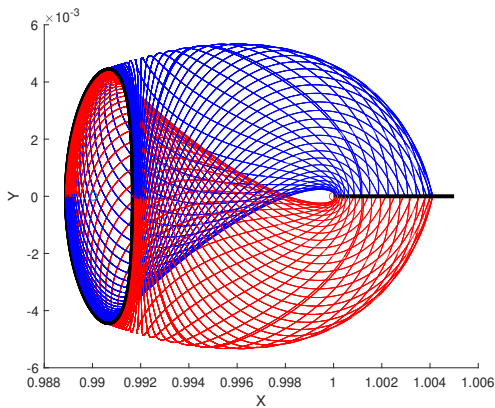


Figure 2.6: Invariant manifolds of the SOHO L1 Halo orbit

Due to the converging nature of the stable manifolds, they can be used for very low energy transfers involving Libration points. This application is investigated in the next chapter.

Chapter 3

Computation of Orbits and Transfers

As this thesis is primarily concerned with design of transfer orbits from Earth to the Lagrange Points listed in Table 1.1, design of specific Lagrange Point orbits for mission criteria is not considered and is the topic for another M.S thesis. Generic Lagrange orbits are presented as basis for transfers trajectory design. The methods presented below are applicable regardless of the specific orbit type.

3.1 Differential Correction

Differential correction is a process for solving Boundary Value Problems as Initial Value Problems. The method makes use of the State Transition Matrix (STM), which is related to the flow map. The STM and flow map are denoted as $\Phi(t, x, x_0)$, and $\phi(t, x, x_0)$ respectively[12]. The flow map x_0 to x at some later time, $\phi(t, x, x_0) : x_0 \rightarrow x(t)$. For simplicity, $x(t_k)$ will be denoted as x_k and $x(t)$ will be x .

Therefore, given some dynamical system

$$\dot{\mathbf{x}} = f(\mathbf{x}, t) \tag{3.1}$$

The flow map, $\phi(t, x, x_0)$ is a solution to the system:

$$\frac{d\phi(t, x, x_k)}{dt} = f(\phi(t, x, x_k)) \quad (3.2)$$

Perturbing the initial state x_k by some value δx_k results in difference in the states δx at some time t :

$$\delta x = \phi(t, x, x_k + \delta x_k) - \phi(t, x, x_k) \quad (3.3)$$

A Taylor series expansion to the first order yields

$$\delta x = \frac{\partial \phi(t, x_k)}{\partial x_k} \delta x_k \quad (3.4)$$

The matrix $\frac{\partial \phi(t, x_k)}{\partial x_k}$ is called the State transition (STM) or sensitivity matrix. The STM, $\Phi(t, t_k)$, linearly maps the initial perturbation to the final perturbation. Additionally, the STM is a solution to the variational equations of 3.1:

$$\delta \dot{\mathbf{x}} = \Phi(t, t_k) \delta \mathbf{x}_k \quad (3.5)$$

$$\delta \dot{\mathbf{x}} = \mathbf{D}f(\mathbf{x}) \delta \mathbf{x}_l \quad (3.6)$$

Where $\mathbf{D}f$ is the Jacobian of the flow along some reference trajectory.

$$\mathbf{x} = [x_1 \ x_2 \ \dots \ x_n]^T \quad (3.7)$$

The STM can be written out as:

$$\Phi(t, t_k) = \begin{bmatrix} \frac{\partial x_1}{\partial x_{1,k}} & \frac{\partial x_1}{\partial x_{2,k}} & \cdots & \frac{\partial x_1}{\partial x_{n,k}} \\ \frac{\partial x_2}{\partial x_{1,k}} & \ddots & & \\ \vdots & & \ddots & \\ \frac{\partial x_n}{\partial x_{1,k}} & & & \frac{\partial x_n}{\partial x_{n,k}} \end{bmatrix} \quad (3.8)$$

The STM is therefore the Jacobian of the state x at some time t , with respect to the initial conditions x_k . To use the STM in the differential corrections process, it must be integrated numerically along with the equations of motion. The time derivative of the STM is:

$$\dot{\Phi}(t, t_k) = \mathbf{A}\Phi(t, t_k) \quad (3.9)$$

where \mathbf{A} is from the linearized dynamical equation and represents the Jacobian of the equations of motion in 3.1.

$$\dot{\mathbf{X}} = \mathbf{A}\mathbf{X} \quad (3.10)$$

3.2 Single Shooting

The single shooting method is used to find solutions to the equations of motion for the CRTBP shown in Equation 2.20. Consider that it is desired to find a Lyapunov orbit in the vicinity of the Sun-Earth L1 point. The orbit is symmetric about the $X - Z$ plane, therefore it is only necessary to find half the actual periodic orbit[22]. The integration time for this trajectory is denoted $T/2$. In most literature, the initial conditions for the orbit are presented as

$$\mathbf{x}_0 = [x \ 0 \ 0; 0 \ y \ 0]^T \quad (3.11)$$

There are two components of the initial conditions that are varied, x , and \dot{y} . Where \dot{y} can be either positive or negative. In order to find a symmetric orbit, the \dot{x} and \dot{z} components of the state vector should be zero at $T/2$. This ensures that the trajectory is perpendicular when it pierces the $X - Z$ plane, which is required for the orbit periodicity. The equations of motion can be arranged in state space form as shown in Equation 2.41. Since the initial conditions are $\mathbb{R}^{6 \times 1}$, the STM and \mathbf{A} for any trajectory in the CRTBP will be $\mathbb{R}^{6 \times 6}$. The Jacobian, \mathbf{A} , has the form shown in Equation 2.42.

3.2.1 Constant Time

In the constant time method, the value of $T/2$ is held constant. For this case, an example of an initial condition vector is given as:

$$\mathbf{X} = [x \ y \ z \ \dot{x} \ \dot{y} \ \dot{z}]^T \quad (3.12)$$

The values of y , \dot{x} , and \dot{z} of the initial state (design vector) are held at a constant value of 0. The remaining variables are allowed to vary during the differential correction process. The variables are adjusted using the STM, which is integrated along with the equations of motion. The term $\delta \mathbf{X}$ from Equation 3.4 is a constraint term. Solving Equation 3.4 for the value of \mathbf{x}_k yields the corrections to the initial condition vector, also called the design vector.

$$\mathbf{X}_f = [x_f \ y_f \ z_f \ \dot{x}_f \ \dot{y}_f \ \dot{z}_f]^T \quad (3.13)$$

Using the symmetry argument as above, the values of y_f , x_f , z_f , and \dot{y}_f are not considered. The constraints required for symmetry are

$$\begin{bmatrix} \dot{x}_f \\ \dot{z}_f \end{bmatrix} = \begin{bmatrix} 0 \\ 0 \end{bmatrix} \quad (3.14)$$

Within some prescribed tolerance, they should be equal to zero. The differential correction process drives the constraint vector to zero. Since the constraints above are already required to be zero, the vector doesn't need to be modified. It is populated by the necessary components of the final state vector. The terms of the design vector, $\delta \mathbf{x}$ are calculated using the matrix inversion. Since bm is the Jacobian of the constraint vector with respect to the design vector, it is a square matrix and a normal matrix inversion is used.

$$\delta \mathbf{x}_k = D\mathbf{f}^{-1} \delta \mathbf{x} \quad (3.15)$$

What results is a Newton iteration.

$$\mathbf{x}_{k,i} = \mathbf{x}_{k,i-1} - D\mathbf{f}^{-1} \delta \mathbf{x}_f \quad (3.16)$$

The integration is then performed again, and the process is repeated until the constraint vector meets the requisite tolerance.

3.2.2 Variable Time

In the variable time version, the value of $T/2$ is allowed to vary. The design vector then takes the form

$$X = \begin{bmatrix} \delta x \\ \delta y \\ \delta T/2 \end{bmatrix} \quad (3.17)$$

and the constraint vector is given below.

$$\mathbf{F}(\mathbf{X}) = \begin{bmatrix} \dot{x}_f \\ \dot{z}_f \\ y_f \end{bmatrix} \quad (3.18)$$

Since the time is allowed to vary, it is necessary to specify the final value of y in the constraint vector. This also serves to keep the Jacobian as a square matrix.

$$D\mathbf{f} = \begin{bmatrix} \frac{\partial \dot{x}_f}{\partial x_k} & \frac{\partial \dot{x}_f}{\partial \dot{y}_k} & \frac{\partial \dot{x}_f}{\partial T/2} \\ \frac{\partial \dot{z}_f}{\partial x_k} & \frac{\partial \dot{z}_f}{\partial \dot{y}_k} & \frac{\partial \dot{z}_f}{\partial T/2} \\ \frac{\partial y_f}{\partial x_k} & \frac{\partial y_f}{\partial \dot{y}_k} & \frac{\partial y_f}{\partial T/2} \end{bmatrix} \quad (3.19)$$

The values in the first two columns of the Jacobian are elements of the STM, which can be substituted in. The last column has the time derivatives of the final state.

$$D\mathbf{f} = \begin{bmatrix} \Phi_{4,1} & \Phi_{4,5} & \ddot{x} \\ \Phi_{6,1} & \Phi_{6,5} & \ddot{z} \\ \Phi_{2,1} & \Phi_{4,5} & \dot{y} \end{bmatrix} \quad (3.20)$$

3.3 Multiple Shooting

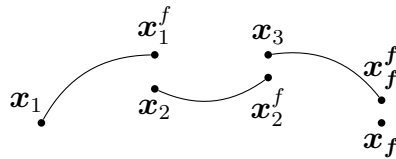


Figure 3.1: Diagram of idea behind the multiple shooting method.

The multiple shooting method is a modification of the single shooting that divides

the trajectory into subsections[25]. The free or design variables are compiled into the design vector, here denoted \mathbf{X} , where $\mathbf{x}_n \in \mathbb{R}^{6 \times 1}$. The design variable vector is therefore of length $6n$.

$$\mathbf{X} = [\mathbf{x}_1 \ \mathbf{x}_2 \ \mathbf{x}_3 \ \mathbf{x}_4 \ \mathbf{x}_5 \ \mathbf{x}_6]^T \quad (3.21)$$

The constraint vector is generally used to ensure continuity along the trajectory at the various patch points.

$$F(\mathbf{X}) = \begin{bmatrix} \mathbf{x}_2^f - \mathbf{x}_2 \\ \mathbf{x}_3^f - \mathbf{x}_3 \\ \mathbf{x}_4^f - \mathbf{x}_4 \\ \mathbf{x}_5^f - \mathbf{x}_5 \\ \mathbf{x}_6^f - \mathbf{x}_6 \end{bmatrix} \quad (3.22)$$

The Jacobian is the derivative of the constraints with respect to the design variables, $\frac{\partial F(\mathbf{X})}{\partial \mathbf{X}} \in \mathbb{R}^{4n \times (4n-1)}$.

$$\frac{\partial F(\mathbf{X})}{\partial \mathbf{X}} = \begin{bmatrix} \frac{\partial(\mathbf{x}_2^f - \mathbf{x}_2)}{\partial \mathbf{x}_1} & \frac{\partial(\mathbf{x}_2^f - \mathbf{x}_2)}{\partial \mathbf{x}_2} & \dots & \frac{\partial(\mathbf{x}_2^f - \mathbf{x}_2)}{\partial \mathbf{x}_n} \\ \vdots & \ddots & & \vdots \\ \frac{\partial(\mathbf{x}_n^f - \mathbf{x}_n)}{\partial \mathbf{x}_1} & & & \frac{\partial(\mathbf{x}_n^f - \mathbf{x}_n)}{\partial \mathbf{x}_n} \end{bmatrix} \quad (3.23)$$

Where each element in $\frac{\partial F(\mathbf{X})}{\partial \mathbf{X}}$ is $\in \mathbb{R}^{6 \times 6}$. Taking, for example, the top left element. It's easy to see that since it is a partial derivative of vectors that each element is it's own Jacobian matrix.

$$\frac{\partial(\mathbf{x}_2^f - \mathbf{x}_2)}{\partial \mathbf{x}_1} = \frac{\partial \mathbf{x}_2^f}{\partial \mathbf{x}_1} - \frac{\partial \mathbf{x}_2}{\partial \mathbf{x}_1} \quad (3.24)$$

Some important properties are noticeable after some simplification.

- $\frac{\partial \mathbf{x}_2}{\partial \mathbf{x}_1} = 0$, since \mathbf{x}_2 has no dependence on \mathbf{x}_1
- $\frac{\partial \mathbf{x}_2}{\partial \mathbf{x}_2} = \mathbf{I}_{6 \times 6}$
- $\frac{\partial (\mathbf{x}_n^f - \mathbf{x}_n)}{\partial \mathbf{x}_n} = \Phi(t_{i+1}, t)$, the state transition matrix for that particular arc

$$\frac{\partial F(\mathbf{X})}{\partial \mathbf{X}} = \begin{bmatrix} \Phi_1 & -\mathbf{I}_{6 \times 6} & \mathbf{0} & \dots & \mathbf{0} \\ \mathbf{0} & \ddots & \ddots & & \\ \vdots & & \ddots & \ddots & \\ \mathbf{0} & & & \Phi_n & -\mathbf{I}_{6 \times 6} \end{bmatrix} \quad (3.25)$$

It's often useful to include time in the design variable. Defining t_n as the integration time for the n th arc of the multiple shooting method, the design vector takes the form below.

$$\mathbf{X} = \begin{bmatrix} \mathbf{x}_1 \\ \mathbf{x}_2 \\ \vdots \\ \mathbf{x}_n \\ t_1 \\ t_2 \\ \vdots \\ t_n \end{bmatrix} \quad (3.26)$$

The constraint vector remains unchanged, resulting in a Jacobian matrix $\frac{\partial F(\mathbf{X})}{\partial \mathbf{x}} \in \mathbb{R}^{7(n-1) \times 6n}$

$$\frac{\partial F(\mathbf{X})}{\partial \mathbf{X}} = \begin{bmatrix} \Phi_1 & -\mathbf{I}_{6 \times 6} & \mathbf{0} & \dots & \mathbf{0} & \dot{\mathbf{x}}_1 \\ \mathbf{0} & \ddots & \ddots & & & \dot{\mathbf{x}}_2 \\ \vdots & & \ddots & \ddots & & \ddots \\ \mathbf{0} & & & \Phi_n & -\mathbf{I}_{6 \times 6} & \dot{\mathbf{x}}_n \end{bmatrix} \quad (3.27)$$

3.4 Targeting Halo Orbits

3.4.1 Lyapunov

Lyapunov orbits exist in the ecliptic plane and are symmetric about the X-Z plane. These properties lead to a formulation for an initial state estimate:

$$\mathbf{x}_0 = [x \ 0 \ 0 \ 0 \ \dot{y} \ 0]^T \quad (3.28)$$

To ensure symmetry, the orbit should pierce the X-Z plane with $\dot{x} = 0$ and $\dot{z} = 0$. Using the single shooting method, the constraint vector is:

$$F(\mathbf{X}) = \begin{bmatrix} y_f \\ \dot{x}_f \\ \dot{z}_f \end{bmatrix} \quad (3.29)$$

As implied in Equation 3.28, the only elements of the state vector allowed to vary are x and \dot{y} . These make up the first two entries in the design vector. The last entry in the design vector is $T/2$.

$$\mathbf{D} = \begin{bmatrix} x_0 \\ \dot{y}_0 \\ T/2 \end{bmatrix} \quad (3.30)$$

The Jacobian is then

$$\mathbf{DF} = \begin{bmatrix} \frac{\partial y_f}{\partial x_0} & \frac{\partial y_f}{\partial \dot{y}_0} & \frac{\partial y_f}{\partial T/2} \\ \frac{\partial \dot{x}_f}{\partial x_0} & \frac{\partial \dot{x}_f}{\partial \dot{y}_0} & \frac{\partial \dot{x}_f}{\partial T/2} \\ \frac{\partial \dot{z}_f}{\partial x_0} & \frac{\partial \dot{z}_f}{\partial \dot{y}_0} & \frac{\partial \dot{z}_f}{\partial T/2} \end{bmatrix} \quad (3.31)$$

The first two columns are entries from the State Transition Matrix, and the last column is comprised of entries from the derivative of the state vector at $T/2$.

$$\mathbf{Df} = \begin{bmatrix} \Phi_{2,1} & \Phi_{2,5} & \dot{y}_f \\ \Phi_{4,1} & \Phi_{4,5} & \ddot{x}_f \\ \Phi_{6,1} & \Phi_{6,5} & \ddot{z}_f \end{bmatrix} \quad (3.32)$$

Since the Jacobian is a square matrix, the Newton Scheme used is

$$\mathbf{X}_i = \mathbf{X}_{i-1} - \mathbf{Df}^{-1} \mathbf{F}(\mathbf{X}) \quad (3.33)$$

Applying the Newton iteration scheme, given sufficiently good initial conditions, convergence should occur in just a few steps.

Using the multiple shooting method requires modification of the general Multiple Shooting method described in 3.3. First, since only x_0 and \dot{y}_0 are allowed to vary, the remaining elements of the initial state vector are removed from the design vector. Second, since y_f , \dot{x}_f , and \dot{z}_f are the only elements of the final state vector being constrained, the rest must be removed from the constraint vector. Finally, in order to ensure that the y intercept is considered from the correct direction, an inequality constraint is introduced.

$$\dot{y}_f \geq 0; \quad (3.34)$$

Since the multiple shooting method finds the zero, the inequality must be written in the form $f(x) = 0$. For this reason, a slack variable β is introduced.

$$\dot{y}_f - \beta^2 = 0 \quad (3.35)$$

For a multiple shooting method with $n = 3$ patch points, the design vector now consist of x and \dot{y}_0 from the initial state vector, the initial state of the second arc (\mathbf{x}_2), and the slack variable β :

$$\mathbf{X}_0 = [x_0 \ \dot{y}_0 \ \mathbf{x}_2 \ \beta]^T \quad (3.36)$$

Where $\beta > 0$. The first element in the constraint vector remains unchanged, it is still the continuity constraint for the two arcs.

$$F(\mathbf{X}) = \begin{bmatrix} \mathbf{x}_2^f - \mathbf{x}_2 \\ y_f \\ \dot{x}_f \\ \dot{z}_f \end{bmatrix} \quad (3.37)$$

As in Equation 3.27, the diagonal of the Jacobian is made up of elements of the State Transition Matrices for each of the arcs. However, the first and last STM are modified due to the changes in constraint and design vectors. The elements of the first STM included are given as:

$$\Phi_1 = \begin{bmatrix} \frac{\partial x_2^f}{\partial x_0} & \frac{\partial x_2^f}{\partial y_0} \\ \frac{\partial y_2^f}{\partial x_0} & \frac{\partial y_2^f}{\partial y_0} \\ \frac{\partial z_2^f}{\partial x_0} & \frac{\partial z_2^f}{\partial y_0} \\ \frac{\partial \dot{x}_2^f}{\partial x_0} & \frac{\partial \dot{x}_2^f}{\partial y_0} \\ \frac{\partial \dot{y}_2^f}{\partial x_0} & \frac{\partial \dot{y}_2^f}{\partial y_0} \\ \frac{\partial \dot{z}_2^f}{\partial x_0} & \frac{\partial \dot{z}_2^f}{\partial y_0} \end{bmatrix} \quad (3.38)$$

The elements of the last STM included are given as:

$$\Phi_2 = \begin{bmatrix} \frac{\partial y_f}{\partial x_2} & \frac{\partial y_f}{\partial y_2} & \frac{\partial y_f}{\partial z_2} & \frac{\partial y_f}{\partial \dot{x}_2} & \frac{\partial y_f}{\partial \dot{y}_2} & \frac{\partial y_f}{\partial \dot{z}_2} \\ \frac{\partial \dot{x}_f}{\partial x_2} & \frac{\partial \dot{x}_f}{\partial y_2} & \frac{\partial \dot{x}_f}{\partial z_2} & \frac{\partial \dot{x}_f}{\partial \dot{x}_2} & \frac{\partial \dot{x}_f}{\partial \dot{y}_2} & \frac{\partial \dot{x}_f}{\partial \dot{z}_2} \\ \frac{\partial \dot{y}_f}{\partial x_2} & \frac{\partial \dot{y}_f}{\partial y_2} & \frac{\partial \dot{y}_f}{\partial z_2} & \frac{\partial \dot{y}_f}{\partial \dot{x}_2} & \frac{\partial \dot{y}_f}{\partial \dot{y}_2} & \frac{\partial \dot{y}_f}{\partial \dot{z}_2} \\ \frac{\partial \dot{z}_f}{\partial x_2} & \frac{\partial \dot{z}_f}{\partial y_2} & \frac{\partial \dot{z}_f}{\partial z_2} & \frac{\partial \dot{z}_f}{\partial \dot{x}_2} & \frac{\partial \dot{z}_f}{\partial \dot{y}_2} & \frac{\partial \dot{z}_f}{\partial \dot{z}_2} \end{bmatrix} \quad (3.39)$$

The derivative entry correspond to the last arc is:

$$\dot{\mathbf{x}}_f = \begin{bmatrix} \dot{y}_f \\ \ddot{x}_f \\ \ddot{z}_f \end{bmatrix} \quad (3.40)$$

Finally, the Jacobian is:

$$DF = \begin{bmatrix} \Phi_1 & -I_{6 \times 6} & \dot{\mathbf{x}}_2^f & \mathbf{0}_{6 \times 1} \\ \mathbf{0}_{4 \times 2} & \Phi_2 & \mathbf{0}_{6 \times 1} & \dot{\mathbf{x}}_f \end{bmatrix} \quad (3.41)$$

Since the DF is not a square matrix, the newton iteration scheme requires use of a pseudo inverse.

$$\mathbf{X}_i = \mathbf{X}_i - DF^T(DFDF^T)^{-1}F(\mathbf{X}) \quad (3.42)$$

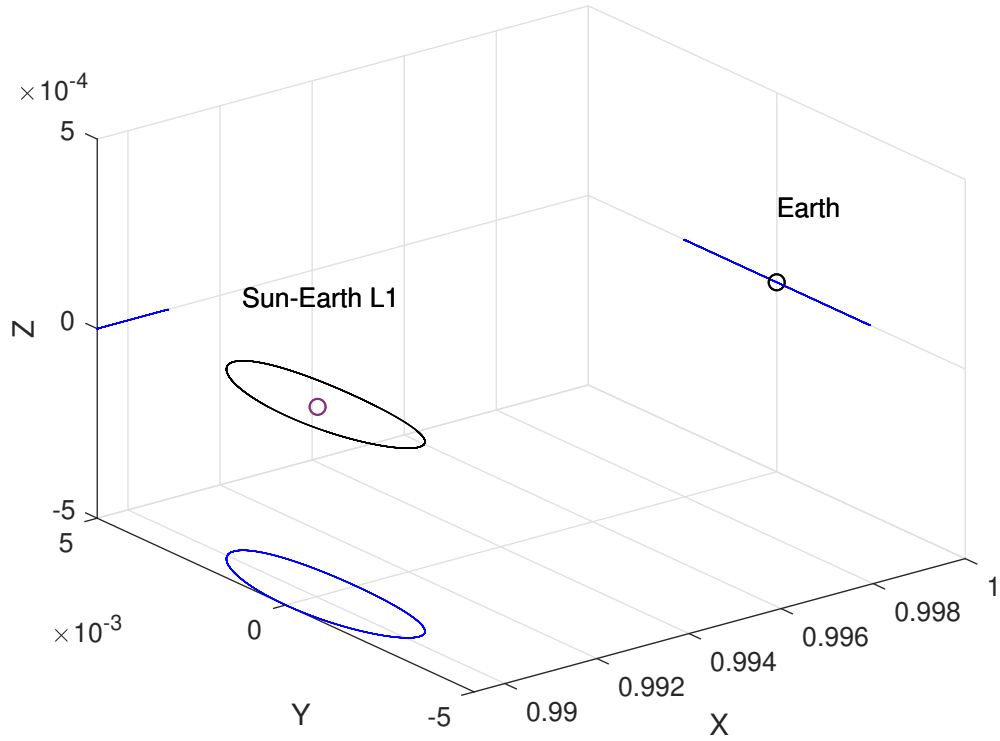


Figure 3.2: Lyapunov Orbit calculated using differential correction.

This iteration results in a least squares solution satisfying the constraints of 3.26 or 3.22.

3.4.2 Halo Orbits

The initial conditions for a Halo orbit are similar to 3.28. However, since Halo orbits are 3 dimensional, they have a z amplitude $A_z > 0$.

$$\mathbf{x}_0 = [x \ 0 \ z \ 0 \ \dot{y} \ 0]^T \quad (3.43)$$

The design vector in the case of the 3D Halo orbit is similar to those in Equation 3.30, however since both x and z are non-zero, the decision of which to include in the design vector and which to hold constant, must be made. In the case where it's necessary to have a specific A_z , it's useful to hold z_0 fixed, so that the differential

correction process doesn't alter A_z . The design and constraint vectors are then exactly the same as in the Lyapunov case.

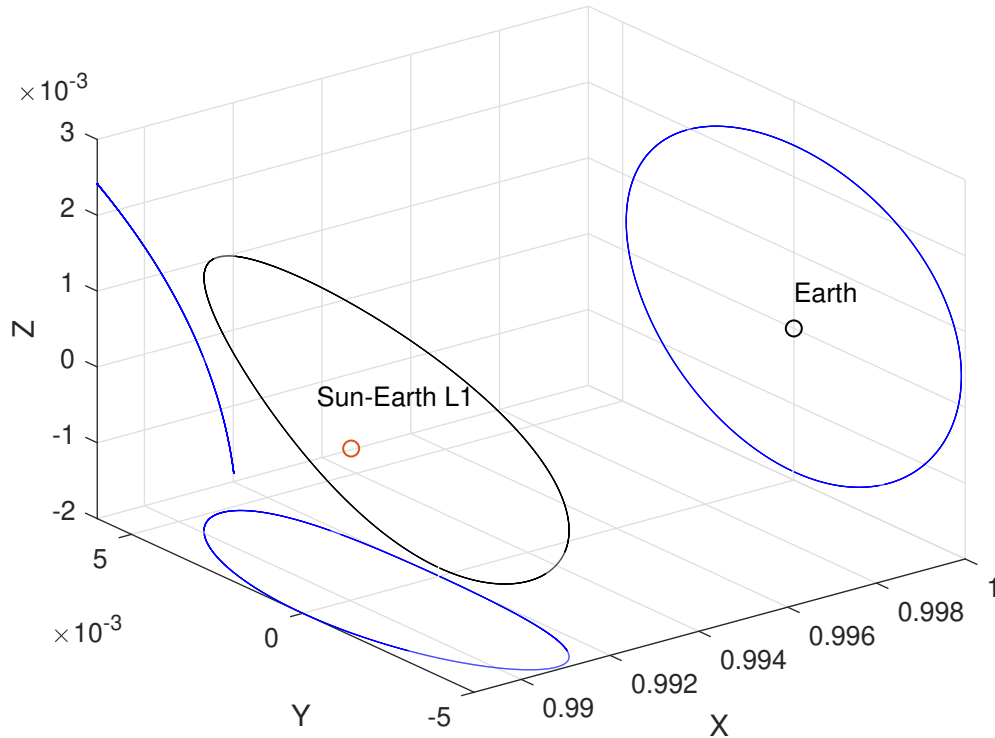


Figure 3.3: Earth L1 Halo Orbit calculated using differential correction method.

3.4.3 Transfers to Libration Point Orbits

Types of Transfers

We will discuss three approaches for transferring spacecraft to their designated Libration point orbit [15, 23].

- Direct Transfer
- Indirect Transfer
- Weak Stability Boundary Transfer

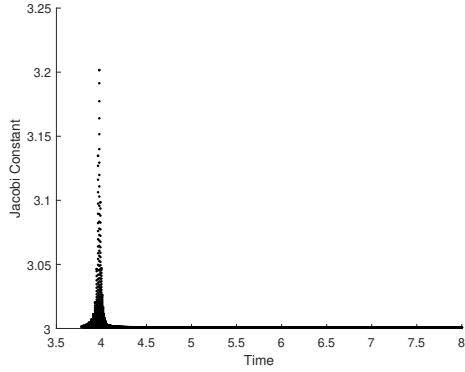
Direct transfers tend to be the most expensive in terms of ΔV , at least when compared to other transfer methods to a libration point orbit. Indirect transfer trajectories make use of the rich dynamics to achieve low thrust transfers to the desired libration point orbit. Weak stability boundary transfer (WSB) also uses invariant manifolds, but may use more than one to achieve the desired orbit [23]. WSB transfer trajectories are typically employed when computing low thrust transfers between LPOs. Research has also been done on using manifolds for interplanetary transfers [22, 25].

In the indirect method a spacecraft is placed on the stable invariant manifold and then drifts to the Halo orbit of that manifold. The trajectory can be divided into three segments [22, 23].

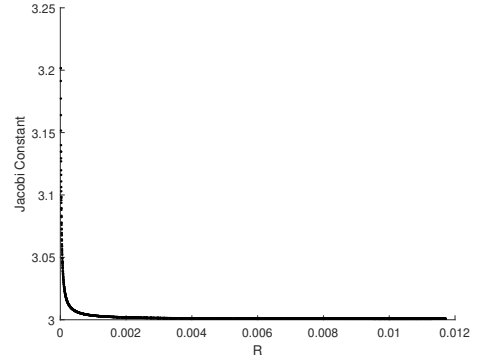
- Transfer Trajectory Insertion (TTI)
- Transfer Trajectory
- Halo Orbit Insertion (HOI)

The TTI will generally take place as an impulsive maneuver from a parking orbit around one of the bodies. Consider the Sun Earth L1 point. By backwards propagating the stable manifold to some area near the Earth (see Figure 2.5), transfer trajectories are naturally found. The issue is then to find some trajectory from parking orbit to the manifold. The single or multiple shooting method can be used here, however since the trajectories are very close to the secondary body; Earth in this case, numerical stability becomes a concern. Since the invariant manifolds are surfaces of constant energy, one way to monitor the numerical error is to calculate the Jacobi constant along each trajectory.

Since the stable manifolds are calculated using backwards integration, the spike in Jacobi Constant values around $t = 4$ is near the end of the integration time span. This coincides with the closet approach to the Earth given a Poincare section at $x = 1 - \mu$. Since the primary and secondary bodies are singularities in the equations of motion, numerical instability in these regions is expected.



(a) Variation of Jacobi Constant as a function of non-dimensional integration time.



(b) Variation of Jacobi Constant as a function of distance to the secondary body, in this case Earth.

Figure 3.4: Jacobi Constant variations during numerical integration with 10th order Runge-Kutta method

Additionally the equation presented by [26] calculates error directly by making use of the monodromy matrix $\Phi(T)$.

$$\epsilon \approx \|\lambda_1\| \epsilon(t_0) \tag{3.44}$$

Here, $\epsilon(t_0)$ is the initial error at the maneuver from parking orbit. For the Halo orbit about the Sun-Earth L2 point with initial conditions as given below, the stable manifold is shown in Figure 3.5

$$\mathbf{x}(t_0) = \begin{bmatrix} 1.01102841501321 \\ 1.1434704 \times 10^{-8} \\ 0.00392014430224348 \\ 7.105861 \times 10^{-9} \\ -0.0107911062813058 \\ -2.55252069 \times 10^{-7} \end{bmatrix} \tag{3.45}$$

Transfer trajectories are found by propagating the stable manifold of an Halo orbit

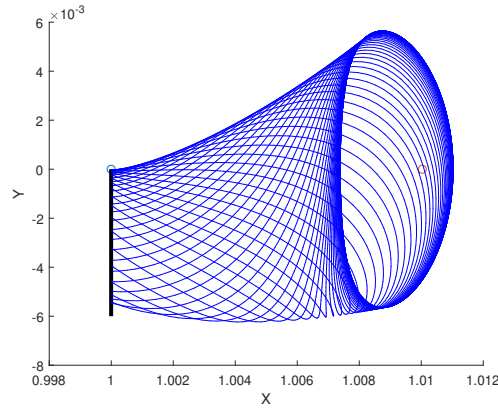
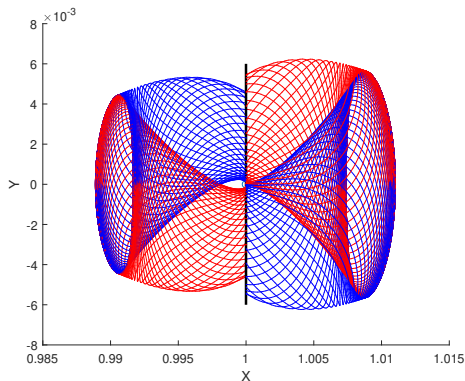
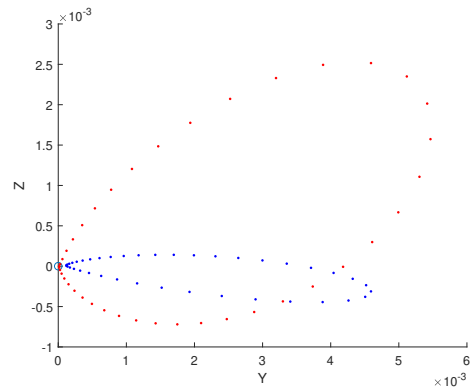


Figure 3.5: Stable manifold of an L2 Halo orbit in the Sun-Earth system

to an appropriate Poincare section. A Poincare section at $y = 0$ and $\dot{y} < 0$ for an L1 insertion and a section of $y = 0$ and $\dot{y} > 0$ for an L2 is recommended [22]. This section should be associated with minimal ΔV cost as the trajectory is tangential to the secondary bodies motion.



(a) Stable and unstable manifolds for L1 and L2 Halo orbits..



(b) Poincare section of the stable manifold from the L1 orbit and the unstable manifold of the L2 orbit.

Figure 3.6: Layout of the weak stability transfer problem.

In Figure 3.6, we can see the Poincare map for the unstable manifold of the L2 LPO overlaps with the Poincare map of the stable manifold of the L1 LPO. A spacecraft can depart the the L2 LPO on the unstable manifold and then perform a ΔV maneuver to transfer onto the stable manifold of the L1 LPO.

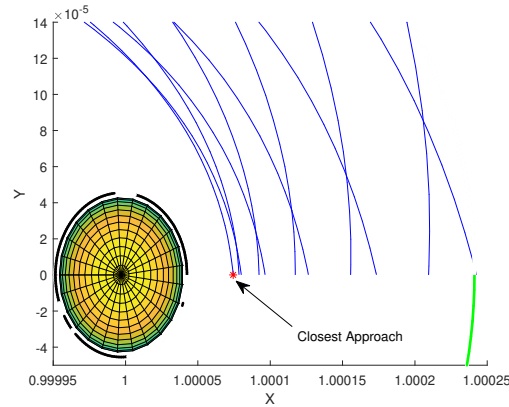


Figure 3.7: Close up view of the Earth and the L1 stable manifold.

Figure 3.7 is a zoomed in view of the stable manifold room an L1 Halo orbit as it approaches the Earth. The point on the Poincare section (not shown) that is closest to the Earth is indicated with a red star. The black circle is an LEO orbit of 400 and the green circle is a GEO orbit of 30,000. A number of trajectories fall within a reasonable range of the Earth, so the closest is arbitrarily chosen as a test point.

For the transfer trajectories discussed, the spacecraft will begin in a parking orbit with the altitude and inclination specific to the manifold trajectory being used. Franco et al. [22] provides a solution to this particular problem using some simple geometry. To find the appropriate parking orbit altitude some point along the manifold surface is chosen. The most intuitive and practical way to do this is to create a Poincare map of the stable manifold at some Poincare section near the Earth. In this case, a planar Poincare section was placed with it's origin at $x = 1 - \mu + 0.01$. The plane was given widths(x) and heights(z) $w = 0.005$ $h = 0.1$. Figure 3.8 illustrates the location of the Poincare section.

The Poincare map generate by this method is display in Figure 3.9. The tube like structure of the invariant manifold is clearly visible. The points in the map can then be iterated through so as to find the one closest to the Earth.

That point will have a state vector in the form

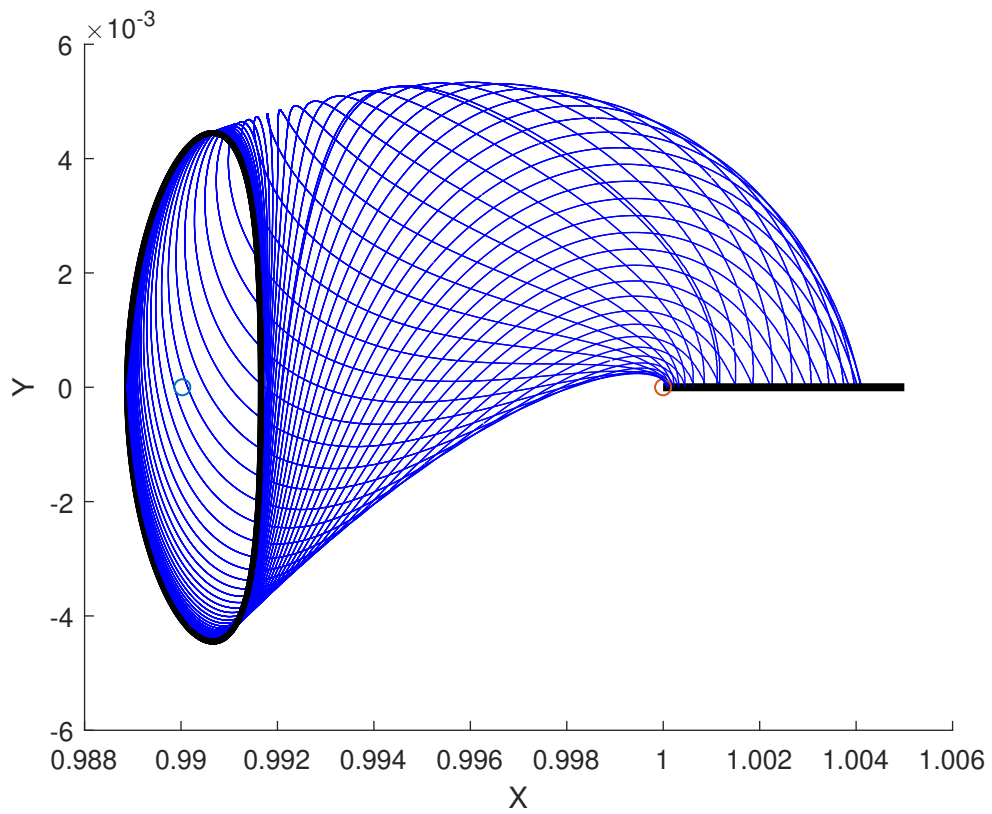


Figure 3.8: Stable manifold propagated back to the Poincare section at $y = 0$

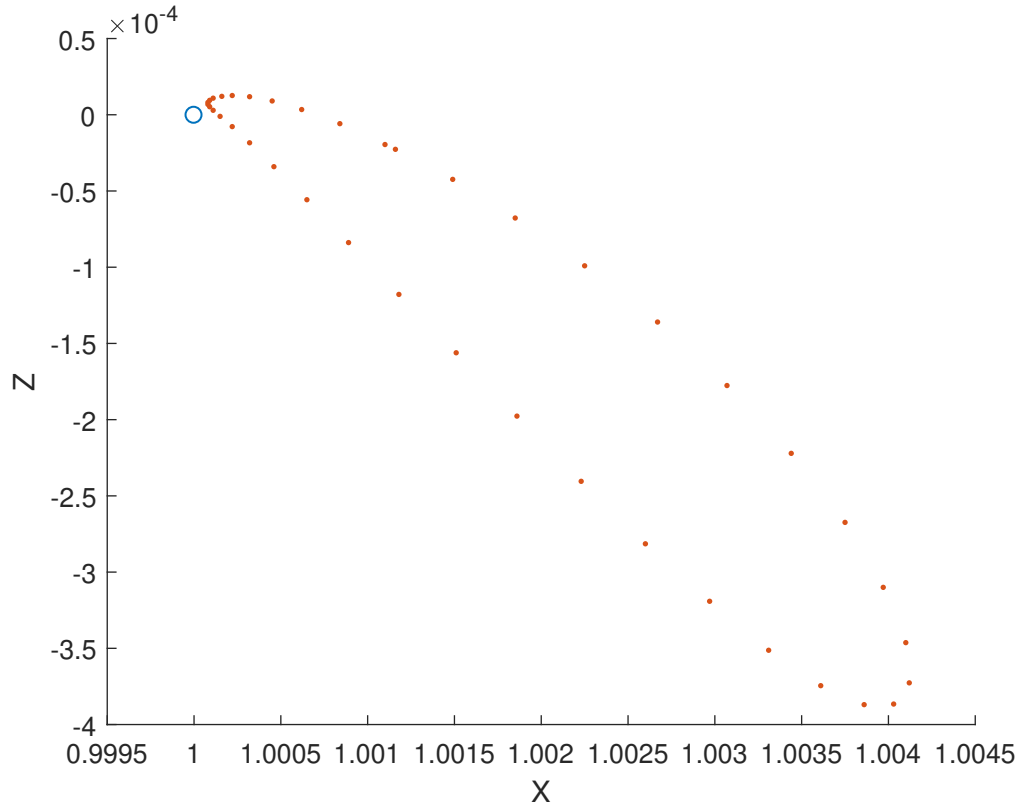


Figure 3.9: Poincare map of the stable manifold at $y = 0$. The blue circle is Earth, orange dots are trajectory intersections with the Poincare section

$$\mathbf{x}_m = [x_m \ y_m \ z_m \ \dot{x}_m \ \dot{y}_m \ \dot{z}_m]^T \quad (3.46)$$

The required parking orbit altitude can be calculated using the following equation [22]

$$h = \sqrt{x_m^2 + y_m^2 + z_m^2} - R_E \quad (3.47)$$

Adding R_E back to h is just the distance of the Poincare map point from Earth. We can find an angle with respect to the ecliptic at which the satellite should be

orbiting [22].

$$i = \text{atan} \left(\frac{z_m}{\sqrt{(x_m - 1 + \mu)^2 + y_m^2}} \right) \quad (3.48)$$

From the Poincare map in Figure 3.9, the closest point to Earth is 8.32805×10^{-5} ; u away. This corresponds to a distance of about 11535 km. The orbit altitude and inclination are then:

$$h = 5156 \text{km} \quad (3.49)$$

$$i = 5.34^\circ \quad (3.50)$$

$$(3.51)$$

These values correspond to a state of:

$$\mathbf{x}_T = [1.00007; 1.96864 \times 10^{-7}; 7.23448 \times 10^{-6} - 0.03161 \ 0.27465; 0.00588] \quad (3.52)$$

The magnitude of velocity for the circular orbit at altitude h is calculated using:

$$v_c = \sqrt{\frac{GM_E}{h + R_E}} \quad (3.53)$$

Which yields an orbital velocity of $v_c = 5.87 \text{km/s}$. The ΔV required to enter the transfer trajectory is then just the difference between the transfer trajectory start point velocity, and the velocity of the circular orbit. The calculated ΔV for this particular transfer (TTI) is $\Delta V = 2.2993 \text{km/s}$

Using the implemented multiple shooting method, targeting Lyapunov and Halo orbits has been done as shown in Figures 1.2 and 3.2. The first figure is a recreation of the SOHO Halo orbit about the Sun-Earth L1. The number of arcs used in the

dividing up up the reference trajectory is configurable. Regardless of the number of arcs chosen, the Jacobian in Equation in 3.27 is built to the correct dimensions and content.

Equation 3.38 is changed to account for the initial positions being held constant, while only the velocities are allowed to vary.

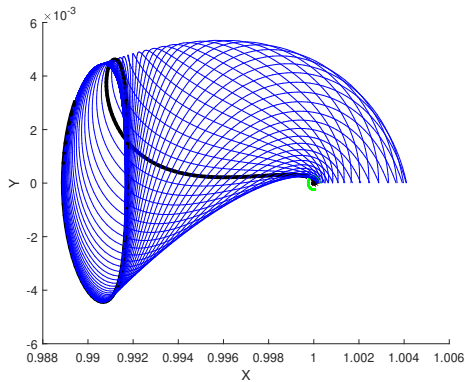
$$\Phi_1 = \begin{bmatrix} \frac{\partial x_2^f}{\partial x_0} & \frac{\partial x_2^f}{\partial y_0} & \frac{\partial x_2^f}{\partial z_0} \\ \frac{\partial y_2^f}{\partial x_0} & \frac{\partial y_2^f}{\partial y_0} & \frac{\partial y_2^f}{\partial z_0} \\ \frac{\partial z_2^f}{\partial x_0} & \frac{\partial z_2^f}{\partial y_0} & \frac{\partial z_2^f}{\partial z_0} \\ \frac{\partial \dot{x}_2^f}{\partial x_0} & \frac{\partial \dot{x}_2^f}{\partial y_0} & \frac{\partial \dot{x}_2^f}{\partial z_0} \\ \frac{\partial \dot{y}_2^f}{\partial x_0} & \frac{\partial \dot{y}_2^f}{\partial y_0} & \frac{\partial \dot{y}_2^f}{\partial z_0} \\ \frac{\partial \dot{z}_2^f}{\partial x_0} & \frac{\partial \dot{z}_2^f}{\partial y_0} & \frac{\partial \dot{z}_2^f}{\partial z_0} \end{bmatrix} \quad (3.54)$$

The last STM in the Jacobian becomes the full STM for that particular arc, if end velocities are being constrained. If only position is being constrained, then the last three rows are removed. The last state derivative entry also has it's acceleration elements removed.

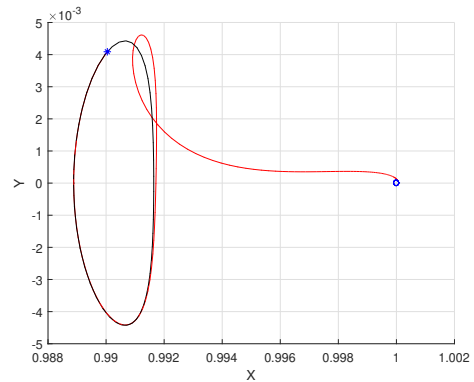
$$\dot{\mathbf{x}}_f = \begin{bmatrix} \dot{x}_f \\ \dot{y}_f \\ \dot{z}_f \end{bmatrix} \quad (3.55)$$

Figures 3.10b and 3.11 illustrate transfer trajectories from Earth and Venus parking orbits. The trajectories were computed using the multiple shooting method described in Section 3.3. Both Halo orbits have Z amplitudes of $A_z = 100000 \text{ km}$. Despite the similar sizes, the transfer trajectories have significantly different ΔV cost for TTI from the parking orbit. The transfer times and ΔV cost for the Earth transfer are similar to those calculated by [22]. The largest difference is in the HOI ΔV .

Since we are primarily concerned with the total time to achieve orbits, it is important to note that the transfer time to Venus L1 does not include time of flight from

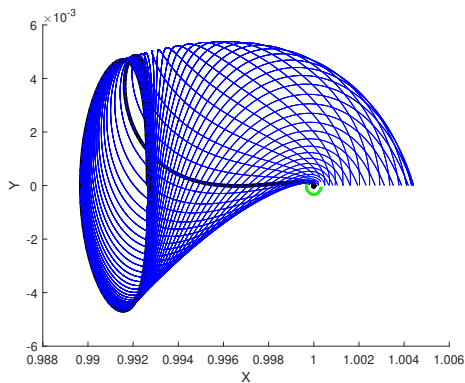


(a) Transfer trajectory to Halo orbit with manifolds indicated.

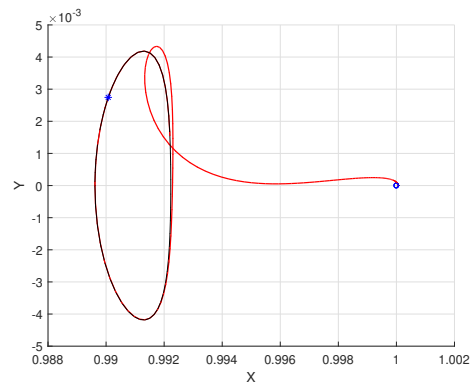


(b) Transfer trajectory to Halo orbit without manifold. HOI is indicated by red star.

Figure 3.10: Transfer orbit from Earth parking orbit to Halo at Sun-Earth L1.



(a) Transfer trajectory to Halo orbit with manifolds indicated.



(b) Poincare section of the stable manifold from the L1 orbit and the unstable manifold of the L2 orbit.

Figure 3.11: Transfer orbit from Venus parking orbit to Halo at Sun-Venus L1.

Earth. There are many types of interplanetary transfers available. Some of those include making use of the unstable manifolds of the departing and target planets. For example in [25], the authors use the unstable manifold of a Sun-Earth-Moon L2 orbit to depart the Earth, and the stable Manifold of a Mars-Sun L1 to enter into Mars orbit. This approach requires finding an intersection of the two manifolds, where a ΔV can be applied to transfer from the Earth unstable to the Mars stable. The same

method could be applied to transfer from Earth to Venus. Instead of departing via the L2 unstable manifold, the spacecraft would depart via the L1 unstable manifold and arrive at Venus via it's L2 stable. Figure 3.12 illustrates this concept. Combining the two CRTBP models requires a non-trivial implementation, and is not attempted as part of this research. However, this technique is worth considering for future work.

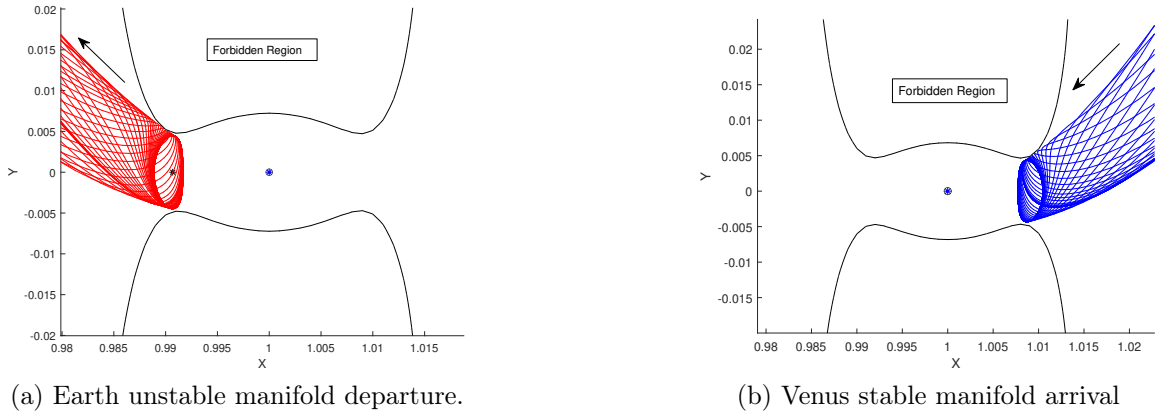


Figure 3.12: Transfer from Earth L1 to Venus L2

In order to obtain a rough estimate of the total transfer time for Venus and Mercury, a Hohmann transfer is considered. The calculations interplanetary Hohmann transfers are described in great detail in [27], and replicated below for this case. In the Hohmann transfer problem, applied to multiple bodies such as in the interplanetary transfer, a patched conic approach is required. This is due to the multiple spheres of influence that the spacecraft must pass through. Spheres of influence are typically defined as regions where a planetary bodies gravitational force is the dominant gravitational force. The radius of these spheres can be calculated using the following equation.

$$R_{SOI} = \left(\frac{GM_p}{GM_s}\right)^{2/5} d \quad (3.56)$$

Where m_p and m_s are the masses of the planet and the sun, and d is the orbital radius of the planet. Table 3.1 summarizes the different SOI for Earth, Venus, and Mercury.

A Hohmann transfer is defined as an elliptical transfer orbit that the spacecraft

Planet	GM($\times 10^6 km^3/s^2$)	Average Orbital Radius($\times 10^6 km$)	SOI Radius($\times 10^5 km$)
Earth	0.39860	149.6	9.24660
Venus	0.32486	108.2	6.16228
Mercury	0.022032	57.91	1.35879

Table 3.1: Spheres of Influence for select planets.

follows to move from one orbit to another. In Figure 3.13, that orbit is shown as "Transfer Trajectory". The arrows indicate the direction of motion of the planets, as well as the departure and arrival velocities. These velocities are defined in the inertial Heliocentric reference frame. The magnitude of velocity of a body orbiting the sun may be calculated using:

$$v = \sqrt{\frac{\mu_{sun}}{a}} \quad (3.57)$$

Where μ_{sun} is the gravitational parameter of the sun and a is the semi-major axis of the orbit. In transferring to the inner solar system, the departing velocity occurs at the apoapsis of the elliptical transfer orbit, and the arriving velocity occurs at the periapsis. Periapsis occurs at the point of closest approach, which is coincident with the semi-major axis of the inner planets orbit. While apoapsis occurs at the furthest point. These two distances can be referred to as R_1 and R_2 . Where R_1 is apoapsis and R_2 is periapsis.

$$v_d = \sqrt{\frac{2\mu_{sun}R_2}{R_1(R_1 + R_2)}} \quad (3.58)$$

$$v_a = \sqrt{\frac{2\mu_{sun}R_1}{R_2(R_1 + R_2)}} \quad (3.59)$$

The relative velocity of required by the satellite after it leaves the Earth's sphere of influence is then calculated:

$$v_r = v_d - v_E \quad (3.60)$$

Since the lowest velocity occurs at apoapsis, these will all result in negative relative

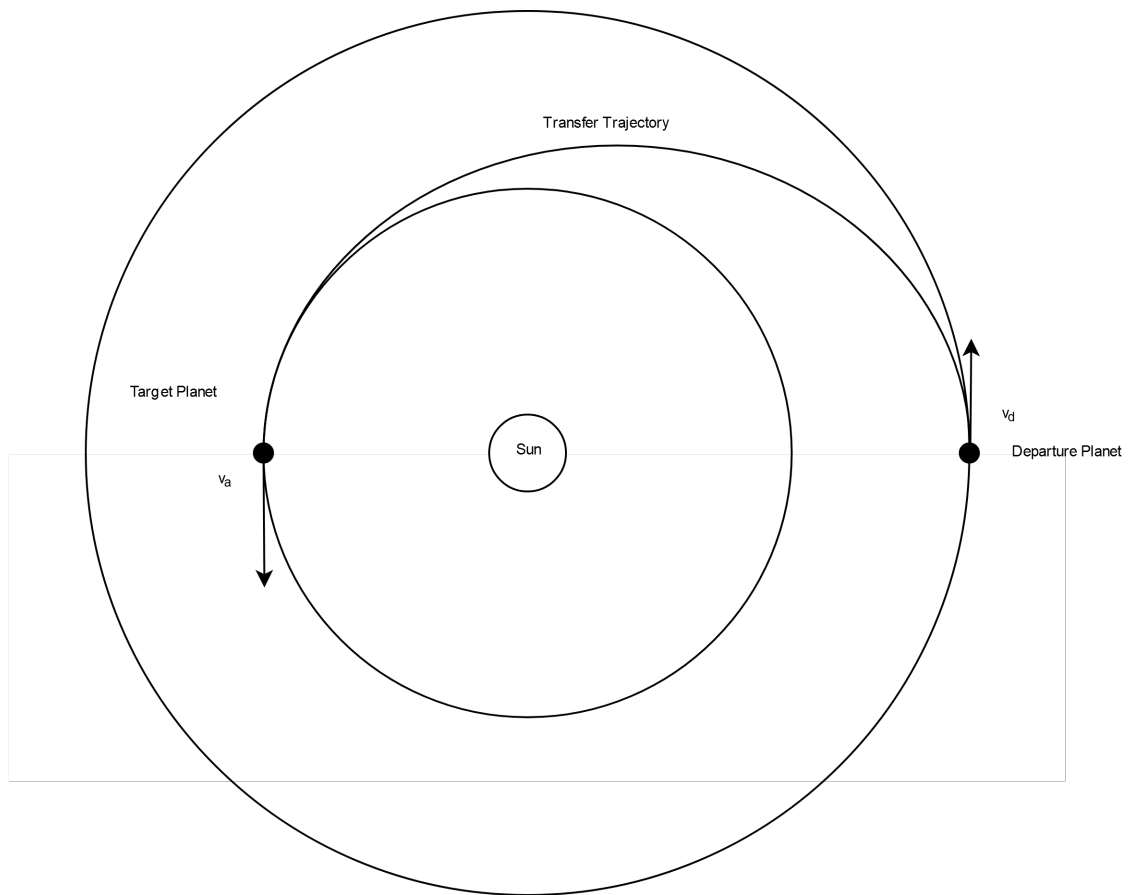


Figure 3.13: Hohmann Transfer

velocities. The spacecraft must lose angular momentum in order to approach the inner planets. Table 3.2 shows values for transfers from Earth to Venus and Mercury.

To achieve these relative velocities, the spacecraft must reach exit the SOI with excess velocity. This excess is the departure relative velocity from Table 3.2. Assuming the spacecraft departs from a circular parking orbit of approximately 400km , the total ΔV required to enter the elliptical transfer orbit can be computed as follows:

$$v_{po} = \sqrt{\frac{\mu_{earth}}{R_{earth} + 400\text{km}}} \quad (3.61)$$

This yields a parking orbit velocity of $v_{po} = 7.67\text{km/s}$. The ΔV to achieve the required hyperbolic departure trajectory is then

Destination	Arrival(<i>km/s</i>)	Departure (<i>km/s</i>)	Arrival Relative (<i>km/s</i>)	Departure Relative (<i>km/s</i>)
Venus	37.73	27.29	2.71	-2.49
Mercury	50.82	22.25	10.12	-7.53

Table 3.2: Velocities for Hohmann Transfers.

$$\Delta v = v_{po} \left(\sqrt{2 + \left(\frac{v_{de}}{v_{po}} \right)^2} - 1 \right) \quad (3.62)$$

Where v_{de} is the excess velocity required. The required ΔV is 3.46km/s for the Earth to Venus transfer, and 5.53km/s for the Earth to Mercury transfer.

The time of flight can be calculated from the following equation:

$$t_{1/2} = \frac{\pi}{\mu_{sun}} \left(\frac{a_d}{a_a} \right)^{3/2} \quad (3.63)$$

The time of flights are then $t_{1/2} = 146.1days$ for Venus, and $t_{1/2} = 105.5days$ for Mercury.

If we consider that the spacecraft depart an Earth parking orbit and enter a parking orbit at either Venus or Mercury, then the total time of flight, assuming a negligible amount of time for entering the correct parking orbit at the target planet, is the transfer time of the elliptical transfer orbit added to the transfer time from parking orbit to the respective L1 point.

Chapter 4

Conclusion

4.1 Implementation

The numerical methods described in Chapters 3 were implemented in the Julia programming language. Julia was chosen for speed and the extensive suite of ODE solvers provided by the `DifferentialEquations.jl` package [28, 29]. One of the key features of this package was its implementation of event detection, which greatly simplifies the calculation of Poincare sections, which are crucial for finding potential initial conditions for transfer orbits. The code was written to be relatively general to allow for reuse wherever possible. In particular the Jacobian created for the multiple shooting method is populated automatically dependent on what boundary values are allowed to vary. A key assumption is that continuity requirements will always include both the position and velocity of the spacecraft.

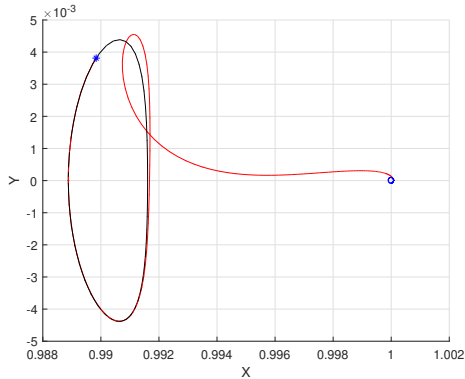
4.2 Results and Discussion

Halo orbits and transfers were generated from 1000km to 150000 km for Earth and Venus, while halo orbits of 1000 km and 100000 km were generated for Mercury. No particular assumptions were made about the parking orbit the spacecraft would be in, other than not allowing the altitude of the orbit to be below the surface of the planet. In order to address stability concerns while integrating near a singularity, such as

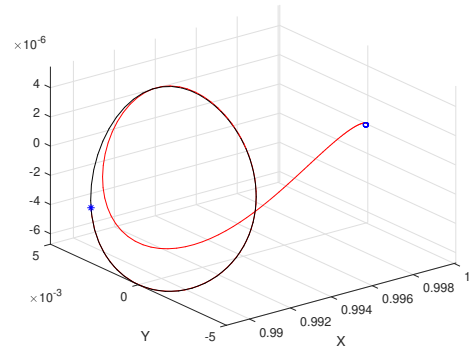
Earth in the CRTBP, the transfer orbits were integrated backwards from the HOI maneuver. The initial conditions for transfer were selected by finding the manifold trajectory that approached closest to the planet. In this case only 40 manifold trajectories were calculated for each orbit, however if further refinement was necessary it is trivial to increase the number of manifold trajectories.

A_z km	Time(days)	TTI ΔV m/s	HOI ΔV m/s
1000	227.14	2360.9	0.0366
50000	227.67	2319.6	0.0366
100000	227.96	2412.1	0.0366
150000	228.65	2575.7	0.0366

Table 4.1: Sample of transfers to varying size Halo orbits at Sun-Earth L1



(a) Top down view of transfer orbit



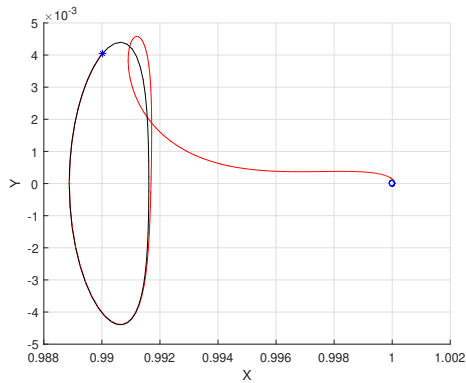
(b) 3D view of transfer orbit

Figure 4.1: Transfer from Earth parking orbit to L1 Halo, with $A_z = 1,000$ km

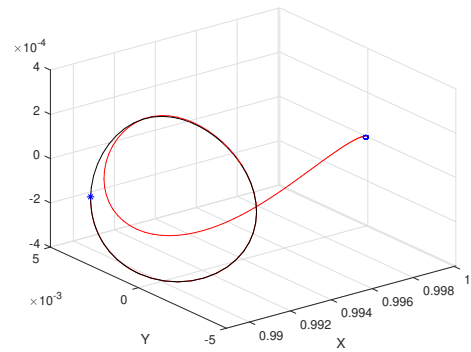
Venus transfer orbits exhibit similar behaviour to the Earth transfer orbits in that they have a constant HOI and a steadily increasing TTI ΔV . However, the transfer times are significantly shorter.

The transfer times shown in Figure 4.3 for Mercury to Sun-Mercury L1 are much shorter than comparable Earth and Venus transfers. The difference in ΔV between the smallest and largest orbit are also quite large.

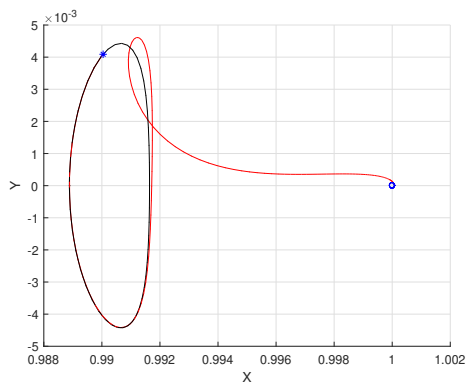
Tables 4.4 and 4.5 summarize transfer times and ΔV for the small 1000 km and the larger 150,000 km orbits. The ΔV requirements are of particular interest as they



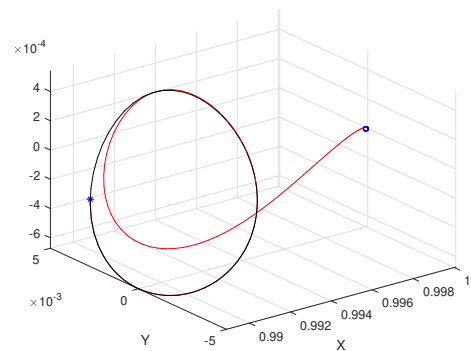
(a) Top down view of transfer orbit



(b) 3D view of transfer orbit

Figure 4.2: Transfer from Earth parking orbit to L1 Halo, with $A_z = 50,000\text{km}$ 

(a) Top down view of transfer orbit



(b) 3D view of transfer orbit

Figure 4.3: Transfer from Earth parking orbit to L1 Halo, with $A_z = 150,000\text{km}$

are exceptionally high. Considering that the MESSENGER spacecraft had a ΔV budget of 2.3 km/s[30], it seems unlikely that a spacecraft on chemical propulsion would be able to achieve the thrust required.

The combined transfer times of Hohmann and Halo orbit trajectories are very reasonable. However, considering the ΔV requirements, it's unlikely that a satellite for this mission would make use of the Hohmann transfer method.

Further research for this mission should involve investigation of interplanetary transfers that make use of Weak-Stability transfers. As discussed in Chapter 3, weak stability transfers can be used to move a satellite between two Halo orbits by exploiting the dynamics of the manifolds. Additionally, the Halo orbits generated can

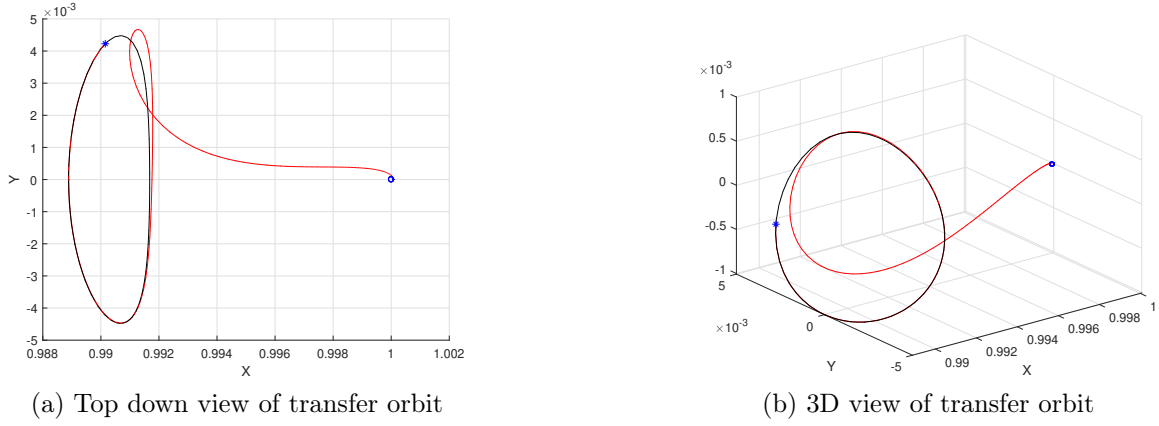


Figure 4.4: Transfer from Earth parking orbit to L1 Halo, with $A_z = 200,000\text{km}$

A_z km	Time(days)	TTI ΔV m/s	HOI ΔV m/s
1000	133.73	2482.59	0.059
50000	133.76	2525.65	0.059
100000	133.92	2656.04	0.059
150000	134.70	3112.91	0.059

Table 4.2: Sample of transfers to varying size Halo orbits at Sun-Venus L1

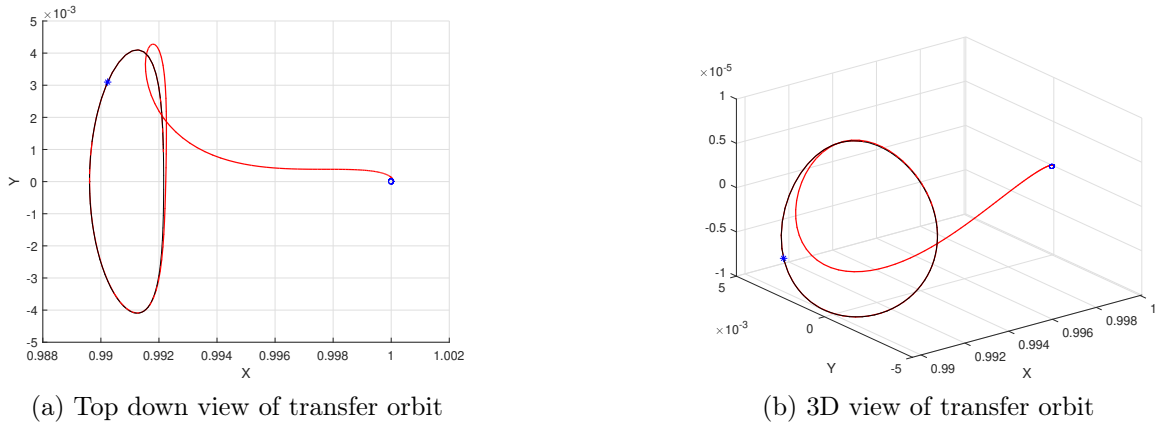
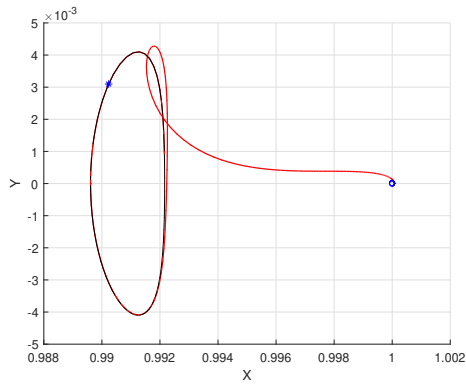
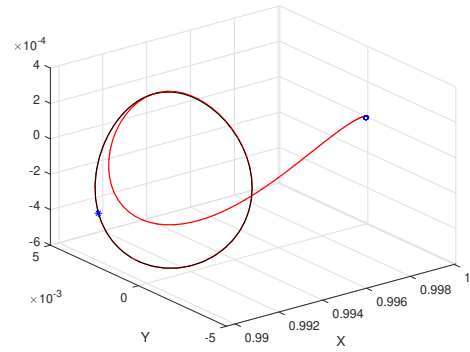


Figure 4.5: Transfer from Venus parking orbit to L1 Halo, with $A_z = 1,000\text{km}$

be further refined by moving from the CRTBP to the Elliptical Restricted Three Body Problem (ERTBP), or the ephemeris model. The ephemeris model makes use of planetary ephemerides generated by the NASA Jet Propulsion Lab to accurately represent planet positions and velocities in three dimensional space. Lagrange point

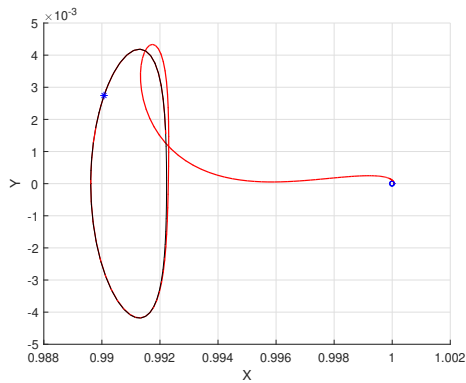


(a) Top down view of transfer orbit

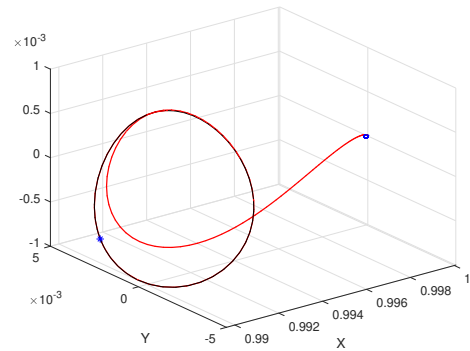


(b) 3D view of transfer orbit

Figure 4.6: Transfer from Venus parking orbit to L1 Halo, with $A_z = 50,000\text{km}$



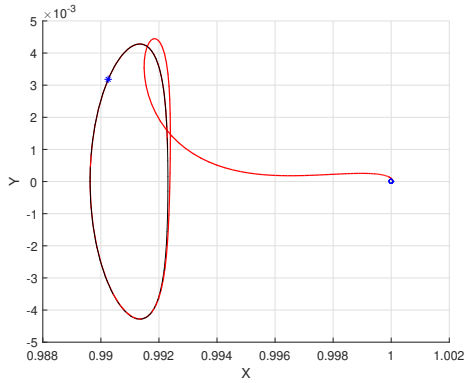
(a) Top down view of transfer orbit



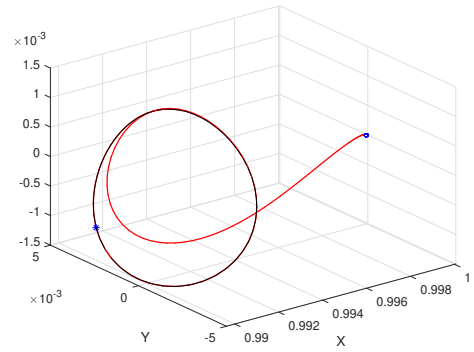
(b) 3D view of transfer orbit

Figure 4.7: Transfer from Venus parking orbit to L1 Halo, with $A_z = 150,000\text{km}$

orbits about L3,L4, and L5 should also be investigated as they are of concern but were not covered as part of this research.



(a) Top down view of transfer orbit

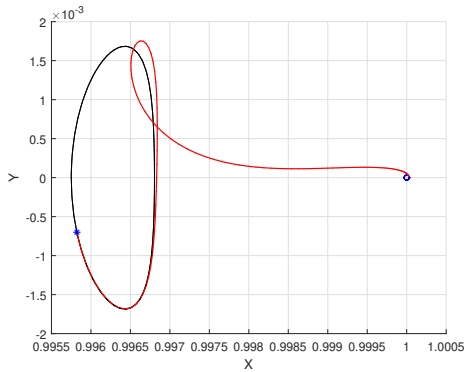


(b) 3D view of transfer orbit

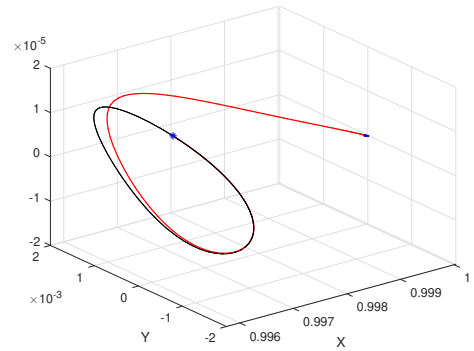
Figure 4.8: Transfer from Venus parking orbit to L1 Halo, with $A_z = 200,000\text{km}$

A_z km	Time(days)	TTI ΔV m/s	HOI ΔV m/s
1000	44.09	1448.18	0.15
150000	45.52	3153.10	0.15

Table 4.3: Sample of transfers to varying size Halo orbits at Sun-Mercury L1



(a) Top down view of transfer orbit

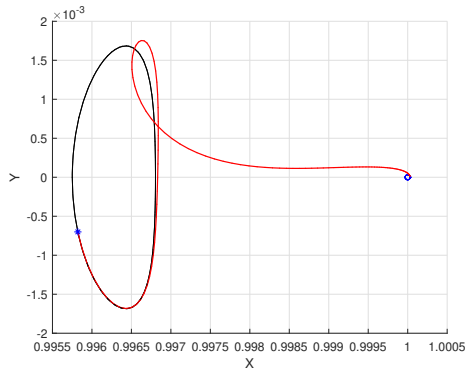


(b) 3D view of transfer orbit

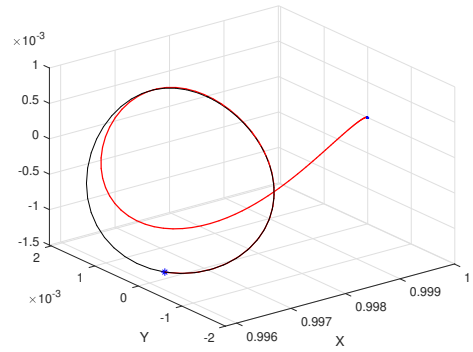
Figure 4.9: Transfer from Mercury parking orbit to L1 Halo, with $A_z = 1,000\text{km}$

Destination	Transfer Time(days)	Total ΔV (km/s)
Venus	279.83	9.24
Mercury	149.59	15.05

Table 4.4: Transfer time and ΔV for Venus and Mercury Halo orbits $A_z = 1000$



(a) Top down view of transfer orbit



(b) 3D view of transfer orbit

Figure 4.10: Transfer from Mercury parking orbit to L1 Halo, with $A_z = 150,000\text{km}$

Destination	Transfer Time(days)	Total ΔV (km/s)
Venus	280.02	9.87
Mercury	151.02	16.75

Table 4.5: Transfer time and ΔV for Venus and Mercury Halo orbits $A_z = 150000$

Bibliography

- [1] C. ROBERTS, “ the Soho Mission L 1 Halo Orbit Recovery From the Attitude Control Anomalies of 1998 ,” pp. 171–217, 2007.
- [2] W. J. Larson and J. R. Wertz, *Space Mission Analysis and Design*, 3rd ed. El Segundo, Ca; Dordrecht, The Netherlands: Microcosm Press; Kluwer Academic Publishers, 2005.
- [3] E. N. Parker, “Dynamics of The Interplanetary Gas and Magnetic Fields,” *American Astronomical Society*, 1958.
- [4] M. Kivelson G and R. T. Christoper, *Introduction to Space Physics*. Cambridge University Press, 1995.
- [5] T. F. Tascione, *Introduction to the Space Environment*, 2nd ed., E. Strother, Ed. Malabar, Fl: Krieger Publishing Company, 1994.
- [6] M. M. Bisi, A. R. Breen, B. V. Jackson, R. A. Fallows, A. P. Walsh, Z. Mikić, P. Riley, C. J. Owen, A. Gonzalez-Esparza, E. Aguilar-Rodriguez, H. Morgan, E. A. Jensen, A. G. Wood, M. J. Owens, M. Tokumaru, P. K. Manoharan, I. V. Chashei, A. S. Giunta, J. A. Linker, V. I. Shishov, S. A. Tyul’bashev, G. Agalya, S. K. Glubokova, M. S. Hamilton, K. Fujiki, P. P. Hick, J. M. Clover, and B. Pintér, “From the Sun to the Earth: The 13 May 2005 coronal mass ejection,” *Solar Physics*, vol. 265, no. 1, pp. 49–127, 1 2010. [Online]. Available: <http://search.proquest.com/docview/746174199/abstract/391645F95C2B4E2DPQ/1http://files/65/Bisietal.-2010-FromtheSuntotheEarthThe13May2005Coronal.pdf>

- [7] T. H. Zurbuchen, M. Weberg, R. V. Steiger, R. A. Mewaldt, S. T. Lepri, and S. K. Antiochos, “COMPOSITION OF CORONAL MASS EJECTIONS,” *The Astrophysical Journal*, vol. 826, no. 1, pp. 1–8, 2016. [Online]. Available: <http://dx.doi.org/10.3847/0004-637X/826/1/10>
- [8] H. Toh, “Real-Time (Quicklook) Dst Index,” 2019. [Online]. Available: http://wdc.kugi.kyoto-u.ac.jp/dst_realtime/index.html
- [9] D. N. Baker, P. J. Erickson, J. F. Fennell, J. C. Foster, A. N. Jaynes, and P. T. Verronen, “Space Weather Effects in the EarthTMs Radiation Belts,” *Space Science Reviews*, vol. 214, no. 1, 2018. [Online]. Available: <http://dx.doi.org/10.1007/s11214-017-0452-7>
- [10] W. Lohmeyer and D. Baker, “Correlation of GEO Comsat Anomalies and Space Weather Phenomena for Improved Satellite Performance and Risk Mitigation,” pp. 1–20, 2013.
- [11] National Oceanic and Atmosphere Administration, “Solar Cycle 25 Preliminary Forecast,” 2019. [Online]. Available: <https://www.swpc.noaa.gov/news/solar-cycle-25-preliminary-forecast>
- [12] M. W. Lo, J. E. Marsden, and S. D. Ross, “<Wang Sang Koon, Martin W. Lo, Jerrold E. Marsden-Dynamical Systems, the Three-Body Problem and Space Mission Design (Interdisciplinary Applied Mathematics) (2009).pdf>.”
- [13] “De motu rectilineo trium corporum se mutuo attrahentium,” *Novi Commentarii academiae scientiarum Petropolitanae*, vol. 11, pp. 144–151, 1767.
- [14] J. L. Lagrange, “Essai sur le Problème des Trois Corps,” *Oeuvres de Lagrange*, vol. 6, pp. 229–332, 1772.
- [15] R. Farquhar, “The flight of ISEE-3/ICE - Origins, mission history, and a legacy,” 2013.

- [16] D. L. Richardson, "Halo Orbit Formulation for the ISEE-3 Mission," *Journal of Guidance, Control, and Dynamics*, vol. 3, no. 6, pp. 543–548, 12 1980. [Online]. Available: <http://arc.aiaa.org/doi/10.2514/3.56033>
- [17] —, "Analytic construction of periodic orbits about the collinear points," *Celestial Mechanics*, vol. 22, no. 3, pp. 241–253, 10 1980. [Online]. Available: <http://link.springer.com/10.1007/BF01229511>
- [18] R. M. Bonnet and F. Felici, "Overview of the SOHO mission," *Advances in Space Research*, vol. 20, no. 12, pp. 2207–2218, 1997.
- [19] P. Sharer and T. Harrington, "Trajectory optimization for the ACE halo orbit mission," pp. 257–267, 2013.
- [20] M. HECHLER and J. COBOS, "Herschel, Planck and Gaia Orbit Design," pp. 115–135, 2007.
- [21] D. A. Vallado, *Fundamentals of Astrodynamics and Applications*, 4th ed. Microcosm Press, 2013.
- [22] A. Franco, B. Zazzera, F. Topputo, M. Massari, P. Milano, and D. Izzo, "Topputo, Bernelli - InterplanetaryHighways-Milano," vol. 31, no. 0.
- [23] P. Kokou, B. Le Bihan, J.-B. Receveur, and S. Lizy-Destrez, "Computing an optimized trajectory between Earth and an EML2 halo orbit," vol. 2014, no. January, 2014.
- [24] H. Zeng and J. Zhang, "Modeling low-thrust transfers between periodic orbits about five libration points: Manifolds and hierarchical design," *Acta Astronautica*, vol. 145, no. January, pp. 408–423, 2018. [Online]. Available: <https://doi.org/10.1016/j.actaastro.2018.01.035>
- [25] M. Kakoi, K. C. Howell, and D. Folta, "Access to Mars from Earth-Moon libration point orbits: Manifold and direct options," *Acta Astronautica*, vol. 102, pp. 269–286, 2014. [Online]. Available: <http://dx.doi.org/10.1016/j.actaastro.2014.06.010>

- [26] Y. Ren and J. Shan, “A novel algorithm for generating libration point orbits about the collinear points,” *Celestial Mechanics and Dynamical Astronomy*, vol. 120, no. 1, pp. 57–75, 9 2014. [Online]. Available: <http://link.springer.com/10.1007/s10569-014-9560-9>
- [27] C. Howard, *Orbital Mechanics for Engineering Students*, 2nd ed. Elsevier Science & Technology, 2009.
- [28] Q. Rackauckas, C. & Nie, “DifferentialEquations.jl â“ A Performant and Feature-Rich Ecosystem for Solving Differential Equations in Julia.” *Journal of Open Research Software*, vol. 5, no. 1, p. 15, 2017.
- [29] “ODE.jl.” [Online]. Available: <https://github.com/JuliaDiffEq/ODE.jl>
- [30] A. G. Santo, R. E. Gold, R. L. McNutt, S. C. Solomon, C. J. Ercol, R. W. Farquhar, T. J. Hartka, J. E. Jenkins, J. V. McAdams, L. E. Mosher, D. F. Persons, D. A. Artis, R. S. Bokulic, R. F. Conde, G. Dakermanji, M. E. Goss, D. R. Haley, K. J. Heeres, R. H. Maurer, R. C. Moore, E. H. Rodberg, T. G. Stern, S. R. Wiley, B. G. Williams, C. W. L. Yen, and M. R. Peterson, “The MESSENGER mission to Mercury: Spacecraft and mission design,” *Planetary and Space Science*, vol. 49, no. 14-15, pp. 1481–1500, 2001.